Single-particle and collective excitations in the $N = 28$ isotones ^{54}Fe and ^{53}Mn

D. Rudolph,[1,*] I. Ragnarsson,[1] C. Andreoiu,[1,2] M. A. Bentley,[3] M. P. Carpenter,[4] R. J. Charity,[5] R. M. Clark,[6] J. Ekman,[1,7] C. Fahlander,[1] P. Fallon,[6] W. Reviol,[4,5] D. G. Sarantites,[5] and D. Seweryniak[4]

[1]*Department of Physics, Lund University, S-22100 Lund, Sweden*
[2]*Chemistry Department, Simon Fraser University, Burnaby, British Columbia, V5A 1S6, Canada*
[3]*Department of Physics, University of York, Heslington, York, YO10 5DD, United Kingdom*
[4]*Physics Division, Argonne National Laboratory, Argonne, Illinois 60439, USA*
[5]*Chemistry Department, Washington University, St. Louis, Missouri 63130, USA*
[6]*Nuclear Science Division, Lawrence Berkeley National Laboratory, Berkeley, California 94720, USA*
[7]*Department of Materials Science and Applied Mathematics, Malmö University, S-20506 Malmö, Sweden*

(Received 14 April 2020; accepted 18 June 2020; published 21 July 2020)

The fusion-evaporation reaction $^{32}S + ^{28}Si$ at 125 MeV beam energy was used to populate high-spin states in the semimagic $N = 28$ nuclei ^{53}Mn and ^{54}Fe. With a combination of the Gammasphere spectrometer and ancillary devices including the Microball CsI(Tl) array, extensive high-spin level schemes are derived. They exhibit rotational-like collective structures and competing single-particle excitations. The experimental results are compared with predictions from shell-model calculations, for which the inclusion of isopin-symmetry-breaking terms is found to improve the description. An interpretation of the high-spin states is put forward using cranked Nilsson-Strutinsky calculations, indicative of contributions from collective excitations beyond some 8-MeV excitation energy and highlighting the importance of the $g_{9/2}$ intruder orbital in this energy range.

DOI: 10.1103/PhysRevC.102.014316

I. INTRODUCTION

One of many facets that mark doubly-magic nuclei as cornerstones on the nuclear chart is the coexistence of spherical and deformed shapes at given excitation energies and angular momenta. While the spherical shape relates to closed shells, multiparticle-multihole excitations across the shell gaps can give rise to significant deformation. Pronounced experimental examples are obtained from the competition between spherical and superdeformed prolate shapes. Such examples were found, for instance, in ^{40}Ca ($N = Z = 20$) [1] and ^{56}Ni ($N = Z = 28$) [2].

The observation and description of this nuclear structure aspect is particularly relevant for the light- and medium-mass doubly-magic nuclei, because they are amenable to various shell-model approaches as well as mean-field methods. This allows one to examine a given nuclear structure model, establishing key parameters, and at the same time conduct comparisons among the different model predictions (see, e.g., Refs. [2–6]).

The rotational bands in ^{56}Ni and its heavier $N \geqslant 28$, $Z \geqslant 28$ neighbors are based on four-particle–four-hole (4p-4h) excitations across the shell gap at particle number 28. This implies particle excitations from the $f_{7/2}$ orbit below $N, Z = 28$ into the $p_{3/2}$, $f_{5/2}$, and $p_{1/2}$ orbits above $N, Z = 28$, forming the so-called upper-fp shell. In addition, promotion of upper-fp-shell particles further into the $g_{9/2}$ intruder orbital leads to increasing prolate deformation, manifested by very rich high-spin level schemes of, for instance, ^{58}Ni [7] or ^{59}Cu [8]. It is noteworthy that some exceptional bands comprise record-breaking discrete states at excitation energies beyond 40 MeV and rotational frequencies in excess of $\hbar\omega > 2$ MeV [9,10].

Because of the relatively low level density of the Nilsson orbitals relevant for mass $A \approx 60$ nuclei, the vast majority of rotational bands with $N, Z \geqslant 28$ can be classified rather easily [8]. This allows for comprehensive investigations of Nilsson model parameterizations [11] and thus improved predictions for the observed rotational bands. In turn, experimental information on this class of rotational bands is scarce in the regime $N, Z < 28$: For example, many rotational structures were observed in the semimagic $Z = 28$ Ni isotopes, but none are known in the $N = 28$ isotones. Nevertheless, evidence for a $g_{9/2}$ rotational band in ^{51}Mn ($N = 26$) has been put reported [12], and shape coexistence is readily predicted for $Z < 28$, $N = 28$ nuclei such as ^{54}Fe [3].

The present study aims at the identification of deformed multiparticle-multihole high-spin states in the $N = 28$ semimagic isotones ^{54}Fe and ^{53}Mn. They are expected to compete with near-spherical states of lower seniority, some of which are known from earlier studies [13–17]. Section II briefly describes the experimental background, and Sec. III summarizes tools and methods of the data analysis. The experimental results are reported in Sec. IV. Section V presents an interpretation of the data in the framework of large-

*Dirk.Rudolph@nuclear.lu.se

scale shell-model calculations and cranked Nilsson-Strutinsky assessments.

II. EXPERIMENT

The data set used for the present study originates from two experiments, which were performed under nearly identical conditions using the Argonne Tandem-Linac Accelerator System at Argonne National Laboratory (ANL) and the 88-inch Cyclotron at Lawrence Berkeley National Laboratory (LBNL). These two experiments employed the fusion-evaporation reaction $^{32}\mathrm{S} + {}^{28}\mathrm{Si}$ at a beam energy of 125 MeV, impinging on the ^{28}Si layer of the target. The ^{28}Si target layers were enriched to 99.90%. They had a thickness of 0.5 mg/cm^2 and they were evaporated onto a 1-mg/cm^2 foil of either tantalum (ANL experiment) or gold (LBNL experiment). These support foils were facing the beam. Excited states in ^{54}Fe and ^{53}Mn were populated following the evaporation, from the compound nucleus ^{60}Zn, of one α particle and two and three protons; i.e., the $1\alpha 2p$ and $1\alpha 3p$ channels were studied.

The target was surrounded by the Gammasphere array [18], which comprised 78 Ge detectors at the time of the experiment. It was used to detect the emitted γ rays. The heavimet collimators were removed to allow for γ-ray multiplicity and sum-energy measurements [19]. Inside the Gammasphere cavity, the 4π CsI-array Microball [20] was mounted, which served to detect the evaporated light charged particles. In addition, the Neutron Shell [21] was used. It consists of 30 liquid-scintillator detectors replacing the 30 most forward Ge detectors of Gammasphere and its primary aim is to discriminate weak reaction channels involving neutron evaporation. Moreover, when studying pure charged-particle evaporation channels, it helps to identify possible contaminations in the data set of interest.

Coincidence events were collected under the condition that either a minimum of four Ge detectors fired, or that valid hits occurred in at least three Ge detectors and one neutron detector. At the end of the experiments, data were taken with ^{56}Co, ^{133}Ba, and ^{152}Eu standard sources to calibrate the Ge detectors. Energy calibrations of Microball detector elements were based on scattering data from $^{12}\mathrm{C}(p, p')$ and $^{197}\mathrm{Au}(\alpha, \alpha')$ reactions.

III. DATA ANALYSIS

The details of the data analysis of this type of experiments have been described earlier; see, for instance, Refs. [22–24] and references therein. In short, γ-ray spectra in prompt coincidence with certain numbers and types of evaporated particles are obtained by employing pulse-shape discrimination techniques to distinguish between protons and α particles detected in Microball and to discriminate between neutrons and γ rays detected in the Neutron Shell. The detection efficiencies for the evaporated particles were determined to be ≈65% for protons, ≈50% for α particles, and ≈25% for neutrons for the present combined data set. An event-by-event kinematic reconstruction method was applied to obtain the momentum vector of the excited residue and subsequently correct the γ-ray spectra for Doppler broadening caused by the evaporated charged particles.

In the course of the analysis E_γ projections, E_γ-E_γ matrices, and E_γ-E_γ-E_γ cubes in coincidence with one α particle and two or three protons were inspected by means of the RADWARE software package [25] and the spectrum-analysis code TV [26]. The $1\alpha 2p$- and $1\alpha 3p$-channel selected E_γ-E_γ matrices served as work horses for the analysis of ^{54}Fe and ^{53}Mn. They comprised approximately 64 and 42 million unfolded $\gamma\gamma$ entries, of which ≈50% and ≈90% were found to originate from ^{54}Fe and ^{53}Mn, respectively. The analysis resulted in the experimental high-spin level schemes of ^{54}Fe and ^{53}Mn shown in Figs. 1 and 2.

Contaminations in the $1\alpha 2p$- and $1\alpha 3p$-gated spectra arise, for example, from the $1\alpha 2p1n$ and $1\alpha 3p1n$ neutron-evaporation channels ^{53}Fe and ^{52}Mn, i.e., when a neutron escapes detection. Very weak contaminations are due to the $4p$ or $5p$ reaction channels ^{56}Fe or ^{55}Mn, i.e., when one or two protons were misidentified as an α particle. Note that only the known main decay sequences of these isotopes are visible in the spectra prepared for the analysis of ^{54}Fe and ^{53}Mn. Second, all these contaminants can be suppressed considerably by applying the total energy plane selection method [27] and by eventually subtracting corresponding spectra in coincidence with, for example, one detected neutron.

Multipolarity assignments of γ-ray transitions were based on directional correlations of oriented states (DCO ratios). The analysis procedure follows the one outlined in Ref. [13] and applied in a number of subsequent publications (see, e.g., Refs. [7,8]). The basis is to combine Gammasphere detectors into four groups of rings: 15 detectors at 163°, 148°, 143° with $\langle\theta_1\rangle = 150°$, 15 detectors at 130° and 122° with $\langle\theta_2\rangle = 127°$, 20 detectors at 110° and 70° with $\langle\theta_3\rangle = 110°$, and 28 detectors at 80–100° with $\langle\theta_4\rangle = 97°$. Note the underlying 90° symmetry of angular distribution and correlation measurements with respect to the reaction plane for fusion-evaporation reactions: For instance, the 10 detectors at 70° and the 10 detectors at 110° can be considered equivalent, $90° \pm 20°$, and they can thus be combined under a common label, here $\langle\theta_3\rangle = 110°$ [13].

DCO ratios are then derived according to

$$R_{\mathrm{DCO}}(150\text{–}97) = \frac{I(\gamma_1 \text{ at } 150°; \text{gated with } \gamma_2 \text{ at } 97°)}{I(\gamma_1 \text{ at } 97°; \text{gated with } \gamma_2 \text{ at } 150°)}.$$

The DCO ratios $R_{\mathrm{DCO}}(150\text{–}127)$ and $R_{\mathrm{DCO}}(127\text{–}97)$ are defined correspondingly.

Known stretched $E2$ transitions ($\Delta I = 2$, $I \to I$–2) were used for gating. In this case, one expects $R_{\mathrm{DCO}} = 1.0$ for observed stretched $E2$ transitions and $R_{\mathrm{DCO}} \approx 0.6$ for stretched pure $\Delta I = 1$, $I \to I - 1$ dipole transitions. Unstretched $\Delta I = 0$ transitions have values similar to $E2$ transitions. If, however, stretched $M1$ transitions were used for gating, $R_{\mathrm{DCO}} \lesssim 1.0$ and $R_{\mathrm{DCO}} \approx 1.6$ is expected for observed stretched $\Delta I = 1$ and $E2$ transitions, respectively. Deviations from the estimates for pure $\Delta I = 1$ transitions indicate a nonzero mixing ratio of the respective transition, namely $\delta(E2/M1) > 0$ (<0) for numbers smaller (larger) than expected for $R_{\mathrm{DCO}}(150\text{–}97)$.

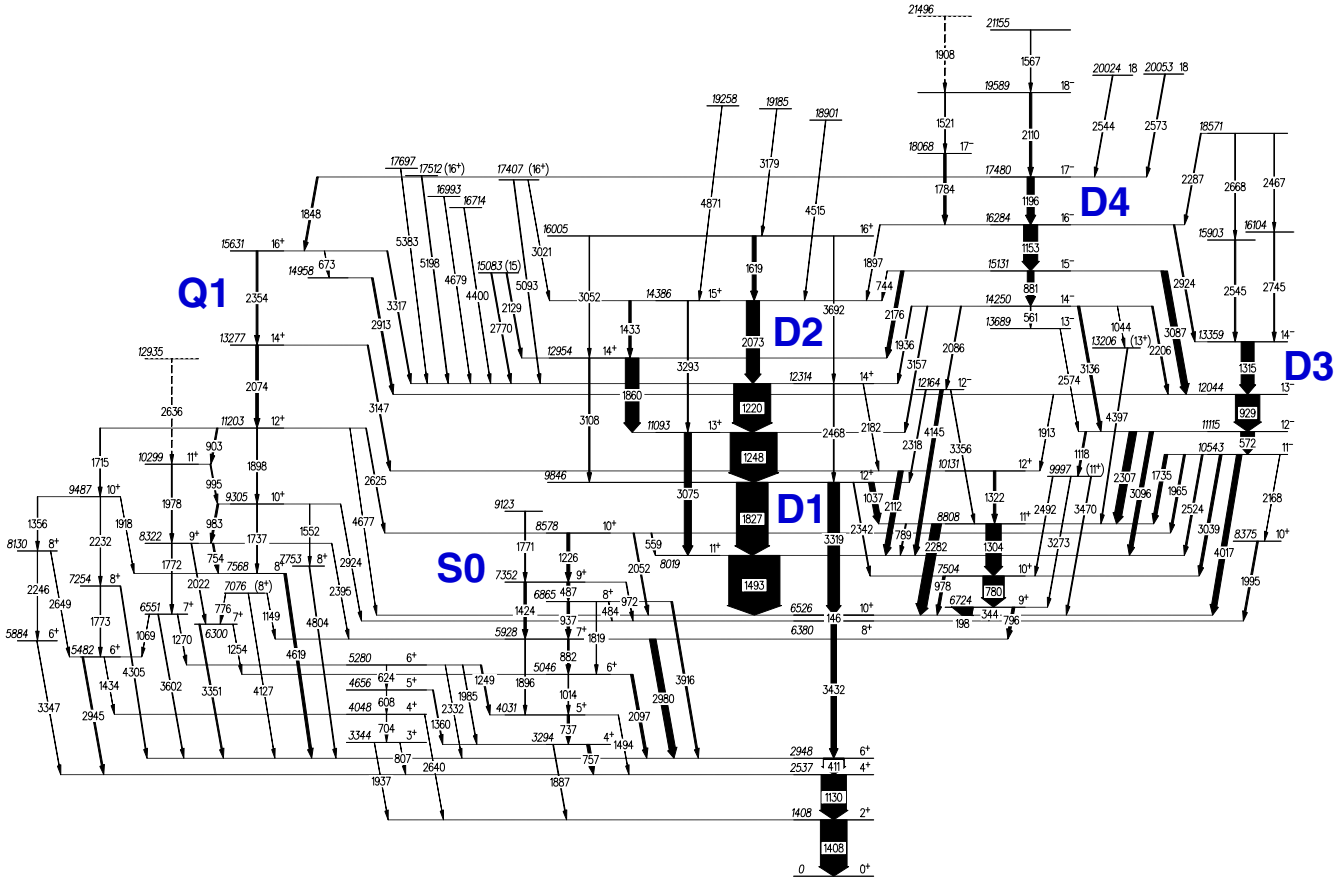

FIG. 1. Proposed high-spin level scheme of ^{54}Fe from the present study. Energy labels are in keV. Tentative transitions and levels are dashed. The widths of the arrows correspond to the relative intensities of the γ rays.

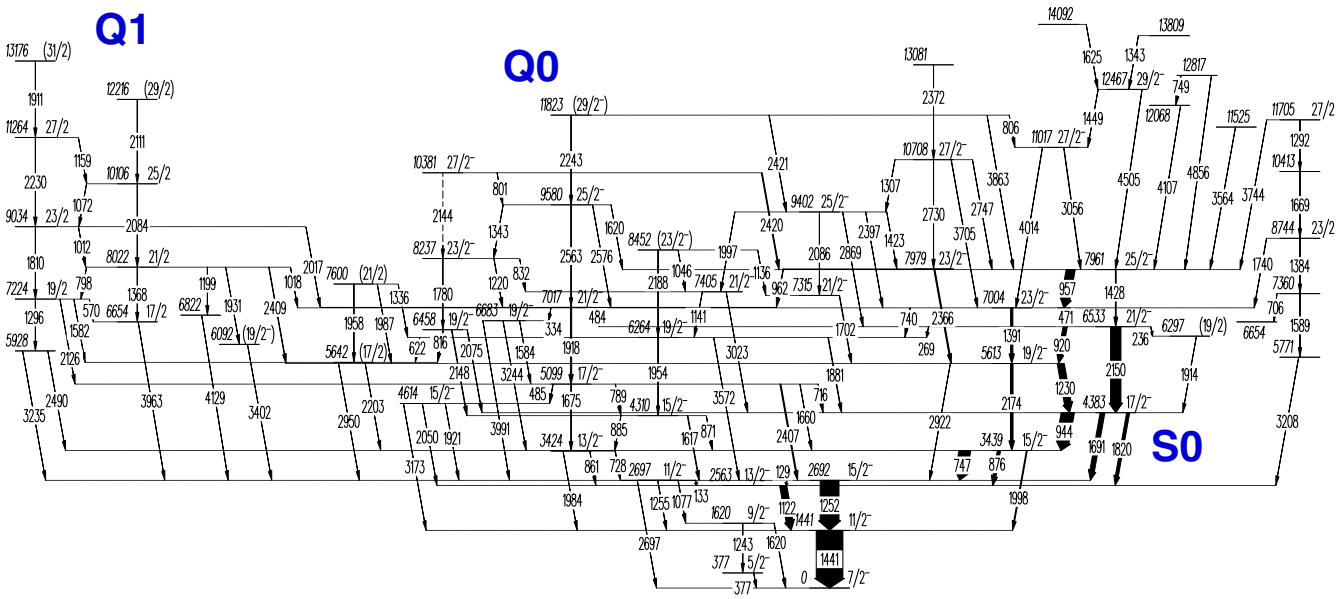

FIG. 2. Proposed high-spin level scheme of ^{53}Mn from the present study. Energy labels are in keV. Tentative transitions are dashed. The widths of the arrows correspond to the relative intensities of the γ rays.

Even though stretched $E2$ and $\Delta I = 0$ transitions provide similar angular distribution and correlation ratios, a distinction is usually straightforward because of yrast arguments—in fusion-evaporation reactions the most intense transitions denote the yrast line—and the combination of the numerical results and sometimes sheer presence of several feeding, decaying, or parallel transitions. A few examples are discussed below.

IV. EXPERIMENTAL RESULTS

Detailed experimental information such as relative intensities and energies of γ-ray transitions as well as excitation energies and spins and parities of observed excited states in ^{54}Fe and ^{53}Mn are collected in Tables I and II. The level schemes of ^{54}Fe and ^{53}Mn (cf. Figs. 1 and 2) have been extended considerably beyond previous work [13–17], while found fully consistent. In ^{54}Fe, the number of γ-ray transitions placed in the level scheme in Fig. 1 could roughly been doubled. The level scheme reveals both hitherto unknown nonyrast sequences and extends the yrast line toward high-spin states beyond 20 MeV excitation energy. The level scheme of ^{53}Mn includes high-spin states at 14 MeV excitation energy and almost ten times more γ-ray transitions than the previous yrast schemes reported in Refs. [15,17]. Because of the additional evaporated and detected proton, the present data set of ^{53}Mn has better signal-to-noise ratio compared to the present ^{54}Fe data set. Hence, for ^{53}Mn one obtains somewhat more precise γ-ray yields (cf. Table II) and thus branching ratios than for ^{54}Fe (cf. Table I). The following presentation focuses on the new experimental findings in the two $N = 28$ isotones.

A. The ^{54}Fe level scheme

The low- to medium-spin yrast sequence of ^{54}Fe is governed by the isomeric 6526-keV 10^+ state with $T_{1/2} = 364(7)$ ns [14] and its well-known $E2$ decay sequence into the

TABLE I. The energies of excited states in ^{54}Fe, the transition energies and relative intensities of the γ rays placed in the level scheme, DCO ratios of three different angle combinations, and the spins and parities of the initial and final states of the γ rays.

E_x (keV)	E_γ (keV)	$I_{\rm rel}$ (%)	Gate[a]	$R_{\rm DCO}$ 150–127°	$R_{\rm DCO}$ 150–97°	$R_{\rm DCO}$ 127–97°	Mult. Ass.	I_i^π ($\hbar$)	I_f^π ($\hbar$)
1407.8(5)	1407.8(5)	1000(30)	B	0.96(5)	0.99(5)	0.94(5)	$E2$	2^+_1[b]	0^+_1
2537.4(6)	1129.5(4)	950(29)	B	0.99(5)	1.03(5)	0.94(5)	$E2$	4^+_1[b]	2^+_1
2948.4(6)	411.1(2)	780(25)	A	1.02(5)	0.96(4)	1.05(4)	$E2$	6^+_1[b]	4^+_1
3294.4(6)	757.0(3)	112(7)	A	0.95(8)	0.91(6)	0.96(7)	$\Delta I = 0$	4^+_2[b]	4^+_1
	1886.9(9)	24(4)					$E2$	4^+_2	2^+_1
3344.1(7)	806.7(5)	8(3)					$E2/M1$	3^+_1[b]	4^+_1
	1936.7(19)	10(3)					$E2/M1$	3^+_1	2^+_1
4031.4(7)	737.0(3)	85(5)	A	0.57(9)	0.40(5)	0.85(9)	$E2/M1$	5^+_1[b]	4^+_2
	1494.1(9)	13(3)					$E2/M1$	5^+_1	4^+_1
4047.7(8)	703.6(6)	12(2)					$E2/M1$	4^+_3[b]	3^+_1
	2640.4(18)	6(3)					$E2$	4^+_3	2^+_1
4655.5(8)	607.9(6)	7(2)					$E2/M1$	5^+_2[b]	4^+_3
	1360.4(7)	33(5)	A	0.84(17)	0.74(12)	0.85(14)	$E2/M1$	5^+_2	4^+_2
5045.7(7)	1014.3(6)	23(3)	A	0.64(21)	0.50(11)	0.49(13)	$E2/M1$	6^+_2[b]	5^+_1
	2097.1(7)	95(4)	C	1.13(15)	1.43(13)	1.24(14)	$\Delta I = 0$	6^+_2	6^+_1
5280.3(7)	624.4(6)	9(3)					$E2/M1$	6^+_3[b]	5^+_2
	1249.4(6)	47(4)	[c]				$E2/M1$	6^+_3	5^+_1
	1985.4(9)	21(5)					$E2$	6^+_3	4^+_2
	2332.2(12)	18(4)					$\Delta I = 0$	6^+_3	6^+_1
5481.6(8)	1433.8(6)	8(3)					$E2$	6^+_4[b]	4^+_3
	2944.6(11)	57(4)	A	0.96(30)	1.00(20)	0.98(22)	$E2$	6^+_4	4^+_1
5884.2(15)	3346.8(20)	14(3)	[c]				$E2$	6^+_5[d]	4^+_1
5927.6(7)	881.9(3)	61(5)	C	0.79(10)	0.71(7)	0.70(8)	$E2/M1$	7^+_1[b]	6^+_2
	1896.4(10)	18(5)					$E2$	7^+_1	5^+_1
	2979.6(10)	241(8)	A	1.29(11)	1.53(11)	1.17(9)	$E2/M1$	7^+_1	6^+_1
6299.9(8)	1253.8(8)	10(3)					$E2/M1$	7^+_2	6^+_2
	3351.2(14)	49(4)	B	1.31(25)	1.71(25)	1.07(16)	$E2/M1$	7^+_2[b]	6^+_1

TABLE I. (*Continued.*)

E_x (keV)	E_γ (keV)	$I_{\rm rel}$ (%)	Gate[a]	$R_{\rm DCO}$ 150–127°	$R_{\rm DCO}$ 150–97°	$R_{\rm DCO}$ 127–97°	Mult. Ass.	I_i^π ($\hbar$)	I_f^π ($\hbar$)
6380.2(7)	3431.6(11)	206(7)	C	0.94(6)	1.13(7)	1.05(6)	$E2$	8^+_1[b]	6^+_1
6526.3(7)	146.1(1)	21(3)	[e]				$E2$	10^+_1[b]	8^+_1
6550.6(9)	1069.2(11)	6(2)					$E2/M1$	7^+_3	6^+_4
	1270.4(10)	21(3)					$E2/M1$	7^+_3	6^+_3
	3602.2(14)	26(3)	C	1.21(32)	1.70(36)	0.75(21)	$E2/M1$	7^+_3	6^+_1
6724.0(7)	197.7(1)	733(24)	E	0.89(5)	0.80(4)	1.14(6)	$E2/M1$	9^+_1[b]	10^+_1
	343.6(3)	2(1)					$E2/M1$	9^+_1	8^+_1
	796.2(3)	99(6)	C	0.95(8)	1.19(9)	1.12(8)	$E2$	9^+_1	7^+_1
			E	1.06(13)	1.57(16)	1.25(12)			
6864.8(7)	484.4(4)	7(2)					$\Delta I = 0$	8^+_2[b]	8^+_1
	937.2(3)	94(6)	C	0.75(7)	0.71(5)	0.85(6)	$E2/M1$	8^+_2	7^+_1
	1819.0(10)	14(3)					$E2$	8^+_2	6^+_2
	3915.9(14)	64(3)	C	1.09(13)	1.16(12)	1.02(11)	$E2$	8^+_2	6^+_1
7076.0(9)	776.0(6)	5(2)					$(E2/M1)$	(8^+_3)	7^+_2
	1149.3(10)	10(3)					$(E2/M1)$	(8^+_3)	7^+_1
	4127.3(21)	12(3)	C	0.91(20)	1.02(19)	0.89(23)	$(E2)$	(8^+_3)	6^+_1
7254.3(11)	1772.6(12)	19(3)	[c]				$E2$	8^+_4[d]	6^+_4
	4305.3(17)	29(2)	C	1.08(27)	1.00(30)	1.13(34)	$E2$	8^+_4	6^+_1
7351.9(8)	487.1(2)	113(4)	C	0.72(5)	0.64(4)	0.85(5)	$E2/M1$	9^+_2[b]	8^+_2
	971.6(6)	22(4)	C	0.70(13)	0.55(7)	0.84(10)	$E2/M1$	9^+_2	8^+_1
	1424.4(5)	90(5)	B	1.09(16)	1.23(14)	1.08(15)	$E2$	9^+_2	7^+_1
7504.1(8)	780.3(3)	802(27)	F	0.86(9)	0.60(6)	0.87(8)	$E2/M1$	10^+_2[b]	9^+_1
			H	0.94(7)	0.98(6)	1.00(6)			
	977.7(4)	93(3)					$\Delta I = 0$	10^+_2	10^+_1
7567.7(8)	4619.4(18)	95(5)	C	1.04(17)	0.92(10)	0.91(10)	$E2$	8^+_5[d]	6^+_1
7752.6(12)	4804.0(22)	28(3)	C	0.95(35)	0.94(26)	0.92(23)	$E2$	8^+_6[d]	6^+_1
8019.3(8)	1492.8(5)	2030(80)	K	0.89(5)	0.94(5)	0.97(5)	$E2/M1$	11^+_1[b]	10^+_1
8130.4(10)	2246.2(16)	9(3)					$E2$	8^+_7[d]	6^+_5
	2648.6(18)	11(3)					$E2$	8^+_7	6^+_4
8322.0(8)	754.3(3)	55(3)	B	0.50(10)	0.55(8)	0.75(10)	$E2/M1$	9^+_3	8^+_5
	1771.6(9)	26(4)					$E2$	9^+_3	7^+_3
	2021.8(9)	25(3)					$E2$	9^+_3	7^+_2
	2394.6(13)	13(2)					$E2$	9^+_3	7^+_1
8375.4(11)	1995.4(9)	62(5)	D	1.00(20)	0.90(17)	0.96(17)	$E2$	10^+_3	8^+_1
8578.3(8)	559.0(2)	36(2)	H	0.85(21)	1.06(27)	1.39(33)	$E2/M1$	10^+_4[b]	11^+_1
	1226.1(5)	111(6)	H	0.79(12)	0.99(12)	0.94(11)	$E2/M1$	10^+_4	9^+_2
	2052.4(7)	47(4)					$\Delta I = 0$	10^+_4	10^+_1
8808.4(8)	788.9(3)	38(3)					$\Delta I = 0$	11^+_2[b]	11^+_1
	1304.3(4)	576(18)	E	1.00(7)	1.19(8)	1.07(6)	$E2/M1$	11^+_2	10^+_2
	2282.4(8)	358(19)	H	1.14(15)	1.25(13)	1.06(12)	$E2/M1$	11^+_2	10^+_1
9123.3(10)	1771.4(7)	35(2)	[c]						9^+_2
9304.6(8)	982.7(4)	65(4)	C	0.57(8)	0.44(6)	0.78(8)	$E2/M1$	10^+_5	9^+_3
	1552.1(11)	3(1)					$E2$	10^+_5	8^+_6
	1736.8(8)	17(2)					$E2$	10^+_5	8^+_5
	2923.8(15)	15(3)					$E2$	10^+_5	8^+_1

TABLE I. (*Continued.*)

E_x (keV)	E_γ (keV)	$I_{\rm rel}$ (%)	Gate[a]	$R_{\rm DCO}$ 150–127°	$R_{\rm DCO}$ 150–97°	$R_{\rm DCO}$ 127–97°	Mult. Ass.	I_i^π ($\hbar$)	I_f^π ($\hbar$)
9486.9(9)	1356.4(7)	18(2)					$E2$	10^+_6[d]	8^+_7
	1918.4(11)	6(2)					$E2$	10^+_6	8^+_5
	2232.2(13)	13(3)					$E2$	10^+_6	8^+_4
9845.5(8)	1037.0(3)	204(13)	K	0.92(10)	0.79(7)	0.79(7)	$E2/M1$	12^+_1[b]	11^+_2
	1826.5(6)	1190(50)	K	0.90(5)	0.92(5)	0.96(5)	$E2/M1$	12^+_1	11^+_1
	2341.8(10)	33(2)					$E2$	12^+_1	10^+_2
	3319.2(11)	439(18)	K	1.08(8)	1.28(9)	1.25(8)	$E2$	12^+_1	10^+_1
9996.6(9)	2492.1(11)	24(2)					$(E2/M1)$	(11^+_3)[g]	10^+_2
	3272.8(18)	21(2)					$(E2)$	(11^+_3)	9^+_1
	3470.4(17)	32(3)					$(E2/M1)$	(11^+_3)	10^+_1
10130.9(9)	1322.4(5)	91(7)					$E2/M1$	12^+_2	11^+_2
	2111.6(8)	188(9)	L	0.93(11)	1.29(13)	1.29(13)	$E2/M1$	12^+_2	11^+_1
10299.4(9)	994.7(4)	36(3)	C	0.53(10)	0.53(8)	0.63(8)	$E2/M1$	11^+_4	10^+_5
	1977.7(8)	32(4)					$E2$	11^+_4	9^+_3
10543.1(8)	1734.5(6)	128(6)	H	1.22(11)	1.74(13)	1.41(11)	$E1$	11^-_1	11^+_2
	1964.8(7)	73(4)	H	0.96(12)	0.91(10)	0.92(10)	$E1$	11^-_1	10^+_4
	2168.1(13)	9(2)					$E1$	11^-_1	10^+_3
	2523.6(8)	62(3)	H	1.07(17)	1.69(24)	1.28(17)	$E1$	11^-_1	11^+_1
	3038.7(10)	97(6)	H	1.04(14)	0.88(9)	0.82(8)	$E1$	11^-_1	10^+_2
	4017.4(15)	203(9)	H	0.81(9)	0.78(6)	0.85(6)	$M2/E1$	11^-_1	10^+_1
11093.4(8)	1247.8(4)	1760(70)	I	0.92(9)	0.72(5)	0.84(6)	$E2/M1$	13^+_1	12^+_1
			K	0.99(6)	1.04(5)	1.04(6)			
	3074.8(10)	267(17)	K	1.20(18)	1.57(19)	1.35(18)	$E2$	13^+_1	11^+_1
11114.7(8)	571.6(2)	521(18)	H	0.90(6)	0.91(5)	0.98(6)	$E2/M1$	12^-_1	11^-_1
	1118.0(7)	62(5)	[c]				$E1$	12^-_1	(11^+_3)
	2306.6(8)	278(13)	E	0.92(11)	1.03(10)	0.96(9)	$E1$	12^-_1	11^+_2
	3096.2(12)	155(9)	[c]				$E1$	12^-_1	11^+_1
11202.6(9)	903.2(4)	53(5)	C	0.77(11)	0.54(7)	0.83(8)	$E2/M1$	12^+_3	11^+_4
			J	0.72(20)	0.54(11)	0.61(14)			
	1715.4(6)	28(2)	J	1.27(38)	0.92(20)	1.18(32)	$E2$	12^+_3	10^+_6
	1898.3(8)	35(4)					$E2$	12^+_3	10^+_5
	2624.9(14)	27(3)					$E2$	12^+_3	10^+_4
	4676.9(28)	6(2)					$E2$	12^+_3	10^+_1
12043.9(8)	929.2(3)	917(32)	H	1.01(6)	1.12(6)	1.01(6)	$E2/M1$	13^-_1	12^-_1
	1912.9(8)	19(2)					$E1$	13^-_1	12^+_2
12164.1(11)	2318.4(15)	34(3)					$E1$	12^-_2	12^+_1
	3356.2(17)	22(3)					$E1$	12^-_2	11^+_2
	4145.2(18)	130(11)	L	1.08(18)	1.08(14)	0.94(12)	$E1$	12^-_2	11^+_1
12313.7(9)	1220.3(4)	1390(50)	G	0.98(10)	0.63(6)	0.81(7)	$E2/M1$	14^+_1	13^+_1
			K	0.98(6)	0.93(5)	0.95(5)			
	2182.4(19)	16(4)					$E2$	14^+_1	12^+_2
	2468.2(11)	28(5)					$E2$	14^+_1	12^+_1
12935.4(20)	2636.0(18)	16(2)							11^+_4
12953.7(9)	1860.3(6)	512(24)	G	0.74(15)	0.57(9)	0.79(14)	$E2/M1$	14^+_2	13^+_1
			K	1.01(10)	0.92(7)	0.98(8)			

TABLE I. (*Continued.*)

E_x (keV)	E_γ (keV)	$I_{\rm rel}$ (%)	Gate[a]	$R_{\rm DCO}$ 150–127°	$R_{\rm DCO}$ 150–97°	$R_{\rm DCO}$ 127–97°	Mult. Ass.	I_i^π ($\hbar$)	I_f^π ($\hbar$)
	3107.8(14)	48(4)					$E2$	14^+_2	12^+_1
13205.7(11)	4397.2(19)	31(2)					$E2$	(13^+_2)[g]	11^+_2
13277.1(10)	2074.4(7)	99(5)	I	1.21(38)	1.48(26)	1.69(31)	$E2$	14^+_3	12^+_3
	3146.7(17)	41(3)					$E2$	14^+_3	12^+_2
13358.8(9)	1314.9(4)	487(22)	H	1.02(7)	1.17(7)	1.13(7)	$E2/M1$	14^-_1	13^-_1
13689.0(9)	2574.2(11)	3(1)					$E2/M1$	13^-_2[h]	12^-_1
14250.1(9)	561.1(3)	22(2)	N	0.80(18)	0.81(12)	0.83(16)	$E2/M1$	14^-_2	13^-_2
	1044.4(7)	4(1)					$E1$	14^-_2	(13^+_2)
	1936.1(9)	34(2)					$E1$	14^-_2	14^+_1
	2086.2(11)	38(5)					$E2$	14^-_2	12^-_2
	2206.3(10)	57(5)	H	1.22(19)	2.01(28)	1.08(14)	$E2/M1$	14^-_2	13^-_1
	3136.3(14)	87(4)	H	1.30(30)	1.92(33)	1.72(33)	$E2$	14^-_2	12^-_1
	3157.1(14)	39(3)	K	0.94(37)	0.99(27)	0.85(24)	$E1$	14^-_2	13^+_1
14386.4(9)	1433.0(7)	88(7)	M	1.23(55)	1.27(25)	1.39(30)	$E2/M1$	15^+_1	14^+_2
	2072.9(7)	495(19)	G	0.89(21)	0.79(14)	0.77(16)	$E2/M1$	15^+_1	14^+_1
			K	1.00(7)	1.15(7)	1.04(6)			
	3292.9(15)	38(4)					$E2$	15^+_1	13^+_1
14957.8(11)	2913.3(13)	62(7)	[c]						13^-_1
15082.8(12)	2128.9(9)	41(3)					$(\Delta I = 1)$	(15)[e]	14^+_2
	2769.5(14)	38(3)					$(\Delta I = 1)$	(15)	14^+_1
15130.6(9)	744.4(6)	6(2)					$E1$	15^-_1	15^+_1
	880.5(3)	252(10)	N	0.95(7)	1.02(7)	1.01(7)	$E2/M1$	15^-_1	14^-_2
	2176.4(9)	126(8)	N	0.87(14)	0.88(9)	0.84(9)	$E1$	15^-_1	14^+_2
	3086.6(12)	241(11)	H	1.08(16)	1.84(22)	1.36(18)	$E2$	15^-_1	13^-_1
15299.5(15)	2986.2(22)[f]	71(4)							14^+_1
	4184.8(23)[f]	10(3)							12^-_1
	4205.9(21)[f]	34(4)							13^+_1
15630.9(10)	673.1(5)	12(2)						16^+_1	
	2353.8(10)	68(4)	J	0.99(19)	1.02(18)	1.10(23)	$E2$	16^+_1	14^+_3
	3316.8(21)	36(5)					$E2$	16^+_1	14^+_1
15903.4(14)	2544.8(13)	50(6)							14^-_1
16005.3(10)	1618.8(5)	148(9)	K	0.90(9)	1.09(9)	1.07(10)	$E2/M1$	16^+_2	15^+_1
	3051.7(15)	19(5)					$E2$	16^+_2	14^+_2
	3692.3(24)	13(4)					$E2$	16^+_2	14^+_1
16103.8(13)	2744.9(11)	35(3)							14^-_1
16115.1(32)	5021.7(31)[f]	18(3)							13^+_1
16283.5(9)	1153.1(5)	531(21)	H	0.94(7)	1.12(7)	1.19(7)	$E2/M1$	16^-_1	15^-_1
			G	0.93(10)	0.74(7)	0.85(8)			
	1897.0(7)	21(3)					$E1$	16^-_1	15^+_1
	2924.4(12)	51(4)	[c]				$E2$	16^-_1	14^-_1
16714.0(28)	4400.3(27)	17(2)							14^+_1
16992.6(30)	4678.9(29)	13(2)							14^+_1
17304.0(19)	3945.4(17)[f]	19(3)							14^-_1
17407.2(19)	3020.8(21)	13(2)					$(E2/M1)$	(16^+)	15^+_1
	5093.3(27)	25(2)	K	1.15(37)	1.80(52)	1.67(47)	$(E2)$	(16^+)	14^+_1

TABLE I. (*Continued.*)

E_x (keV)	E_γ (keV)	$I_{\rm rel}$ (%)	Gate[a]	$R_{\rm DCO}$ 150–127°	$R_{\rm DCO}$ 150–97°	$R_{\rm DCO}$ 127–97°	Mult. Ass.	I_i^π ($\hbar$)	I_f^π ($\hbar$)
17479.5(9)	1196.2(5)	268(11)	N	1.04(10)	1.08(8)	1.03(8)	$E2/M1$	17^-_1	16^-_1
	1848.4(7)	61(3)	J	0.78(22)	0.66(15)	0.78(19)	$E1$	17^-_1	16^+_1
17512.0(28)	5198.3(27)	26(2)	K	1.43(45)	1.80(52)	1.29(35)	$(E2)$	(16^+)	14^+_1
17696.6(34)	5382.9(33)	12(2)							14^+_1
18067.6(11)	1783.8(7)	91(6)	N	0.93(16)	1.22(17)	0.99(12)	$E2/M1$	17^-_2	16^-_1
18570.8(12)	2287.2(11)	32(3)	[c]						16^-_1
	2466.8(14)	5(1)							
	2667.6(15)	9(3)							
18901.4(27)	4515.0(25)	17(3)							15^+_1
19184.5(18)	3179.2(16)	12(4)							16^+_2
19257.7(28)	4871.2(26)	10(2)							15^+_1
19588.7(11)	1520.8(7)	15(2)					$E2/M1$	18^-_1	17^-_2
	2109.6(9)	88(6)	N	1.04(13)	1.19(13)	1.19(14)	$E2/M1$	18^-_1	17^-_1
20023.6(15)	2544.1(11)	27(3)	N	1.10(32)	0.99(18)	0.93(14)	$\Delta I = 1$	18	17^-_1
20052.5(15)	2573.0(11)	34(3)	N	0.93(20)	1.03(16)	0.97(15)	$\Delta I = 1$	18	17^-_1
21155.3(13)	1566.6(7)	19(3)							18^-_1
21496.3(16)	1907.6(12)	10(2)							18^-_1

[a]A, 1408 and 1130 keV; B, 411 keV; C, 1408, 1130, and 411 keV; D, 3432 keV; E, 780 keV (stretched $M1$); F, 796 keV; G, 3075/3087 (doublet) and/or 3319 keV; H, 572 keV and/or 929 keV (stretched $M1$); I, 903 keV (stretched $M1$); J, 2074 keV; K, 1220 keV and/or 1248 keV (stretched $M1$); L, 1493 keV (stretched $M1$); M, 1860 keV (stretched $M1$); N, 1153 keV and/or 1196 keV (stretched $M1$).
[b]Adopted from or consistent with Refs. [13,14].
[c]Doublet structure.
[d]Assignment based on number of stretched $E2$ transitions between states with known spins and parities.
[e]Decay from isomeric state.
[f]Not included in Fig. 1.
[g]Tentative assignment based on yrast arguments.
[h]Assignment based on DCO ratio of feeding transition.

ground state. Because of the isomerism, practically no prompt coincidences are observed across this 10^+ state, which thus collects considerably more γ-ray flux than the ground state, namely more than three times. Already in Ref. [13], γ-ray sequences in prompt coincidence were identified to bypass the isomer.

The positive-parity yrast line on top of the 6526-keV 10^+ isomer the yrast line is determined by an irregular sequence of intense dipole transitions, consistent with Ref. [13] and labeled D1 and D2 in Fig. 1. The lineup 1493-1827-1248-1220-2073-(1860-1433)-1619 keV reaches a hitherto unobserved 16^+ state at 16 MeV excitation energy. Crossover quadrupole transitions are observed but are very weak compared to the dipole transitions. Nevertheless, their observations provides confidence as far as spin-parity assignments are concerned. The DCO ratios and deduced $\delta(E2/M1)$ mixing ratios indicate finite but small $E2$ admixtures for the $\Delta I = 1$ transitions (see Table I). The γ-ray spectra in Fig. 3 illustrate this part of the level scheme, including a number of weak but clearly visible [in Fig. 3(a)] high-energy transitions feeding primarily the yrast 14^+ state at 12314 keV excitation energy.

There are indications of high-energy transitions in Fig. 3(b) at, for example, 3760, 4039, and 4453 keV, which could connect to the states at 16714, 16993, and 17407 keV. However, their yield is too low to unambiguously place them in the level scheme of ^{54}Fe. The same is true for the 3484-keV line in Fig. 3(a). In this group of levels, the only state decaying to both the yrast and yrare 14^+ levels is the one at 15083 keV; the 2770-keV line is clearly visible in Fig. 3(a), and as is the 2129-keV line in Fig. 3(b). Yrast arguments suggest a tentatively assigned spin $I = 15$ to that state. In turn, the DCO ratios deduced for the 5093- and 5198-keV lines are consistent with 16^+ assignments to the states at 17407 and 17512 keV.

Besides the new dipole structure (D4 in Fig. 1) formed primarily by the 881-1153-1196 keV sequence (see below), the γ-ray yield is found to spread out over many (high-energy) transitions at about spin $I = 16$ and excitation energies $E_x \approx$ 16–17 MeV. It is interesting to note that one main decay path of the new dipole sequence passes through the 1860-keV $14^+_2 \rightarrow 13^+_1$ transition, rather than the much more intense 1220 yrast $14^+_1 \rightarrow 13^+_1$ transition: The connecting 2176-keV line as well as those at 1153, 1196, and 1784 keV are clearly seen in Fig. 3(b), while the latter are hardly visible in Fig. 3(a).

The γ-ray spectra in Fig. 4 relate to the previously established [13] sequence of dipole transitions at 572, 929, and

TABLE II. The energies of excited states in ^{53}Mn, the transition energies and relative intensities of the γ rays placed in the level scheme, DCO ratios of three different angle combinations, and the spins and parities of the initial and final states of the γ rays.

E_x (keV)	E_γ (keV)	$I_{\rm rel}$ (%)	Gate[a]	$R_{\rm DCO}$ 150–127°	$R_{\rm DCO}$ 150–97°	$R_{\rm DCO}$ 127–97°	Mult. Ass.	I_i^π ($\hbar$)	I_f^π ($\hbar$)
377.3(2)	377.4(2)	5.4(5)					$E2/M1$	$5/2^-_1$[b]	$7/2^-_1$
1440.9(5)	1441.1(7)	1000(30)	A	0.97(4)	0.95(4)	0.95(4)	$E2$	$11/2^-_1$	$7/2^-_1$
1619.9(4)	1242.6(6)	4.5(8)					$E2$	$9/2^-_1$[b]	$5/2^-_1$
	1619.6(8)	13(1)					$E2/M1$	$9/2^-_1$[b]	$7/2^-_1$
2563.3(5)	1122.4(6)	261(8)	B	0.84(5)	0.59(3)	0.76(4)	$E2/M1$	$13/2^-_1$	$11/2^-_1$
2692.2(5)	128.9(2)	1.5(5)					$E2/M1$	$15/2^-_1$	$13/2^-_1$
	1251.5(6)	706(21)	A	1.02(5)	1.00(4)	1.03(4)	$E2$	$15/2^-_1$	$11/2^-_1$
2696.6(5)	133.4(2)	3.4(4)					$E2/M1$	$11/2^-_2$[b]	$13/2^-_1$
	1076.6(5)	16(1)					$E2/M1$	$11/2^-_2$[b]	$9/2^-_1$
	1255.3(6)	12(1)					$\Delta I=0$	$11/2^-_2$[b]	$11/2^-_1$
	2696.8(13)	6.0(9)					$E2$	$11/2^-_2$[b]	$7/2^-_1$
3424.3(5)	727.6(4)	17(2)	C	0.95(20)	0.30(5)	0.60(10)	$E2/M1$	$13/2^-_2$	$11/2^-_2$
	860.9(4)	3.0(3)					$\Delta I=0$	$13/2^-_2$	$13/2^-_1$
	1984.2(10)	2.6(4)					$E2/M1$	$13/2^-_2$	$11/2^-_1$
3438.8(5)	746.5(4)	430(13)	D	1.08(5)	1.03(4)	1.27(5)	$\Delta I=0$	$15/2^-_2$	$15/2^-_1$
	875.6(4)	118(3)	B	0.55(4)	0.32(2)	0.62(4)	$E2/M1$	$15/2^-_2$	$13/2^-_1$
	1998.1(10)	33(1)	B	0.94(12)	1.03(11)	1.12(14)	$E2$	$15/2^-_2$	$11/2^-_1$
4309.9(6)	871.2(4)	2.6(3)					$\Delta I=0$	$15/2^-_3$	$15/2^-_2$
	885.3(6)	2.3(3)					$E2/M1$	$15/2^-_3$	$13/2^-_2$
	1617.4(8)	22(1)	A	0.91(13)	1.13(13)	1.30(17)	$\Delta I=0$	$15/2^-_3$	$15/2^-_1$
4383.0(6)	943.9(5)	481(14)	D	0.56(3)	0.31(1)	0.59(3)	$E2/M1$	$17/2^-_1$	$15/2^-_2$
	1691.0(8)	173(5)	D	0.46(3)	0.23(2)	0.51(2)	$E2/M1$	$17/2^-_1$	$15/2^-_1$
	1819.9(9)	112(3)	D	0.98(7)	1.07(7)	1.10(7)	$E2$	$17/2^-_1$	$13/2^-_1$
4613.5(6)	1921.0(10)	3.0(10)					$\Delta I=0$	$15/2^-_4$[c]	$15/2^-_1$
	2049.9(10)	5.8(4)					$E2/M1$	$15/2^-_4$[c]	$13/2^-_1$
	3173.1(23)	4.8(6)					$E2$	$15/2^-_4$[c]	$11/2^-_1$
5098.8(6)	485.2(2)	10(1)	E		0.66(13)		$E2/M1$	$17/2^-_2$	$15/2^-_4$
	715.7(4)	11(1)	D	1.01(14)	0.99(12)	1.14(14)	$\Delta I=0$	$17/2^-_2$	$17/2^-_1$
	788.9(4)	10(1)	E		0.26(7)		$E2/M1$	$17/2^-_2$	$15/2^-_3$
	1659.6(8)	8.3(7)					$E2/M1$	$17/2^-_2$	$15/2^-_2$
	1674.6(8)	12(1)	E		1.24(33)		$E2$	$17/2^-_2$	$13/2^-_2$
	2407.2(12)	38(2)	A	0.38(13)	0.28(5)	0.58(6)	$E2/M1$	$17/2^-_2$	$15/2^-_1$
5613.3(6)	1230.1(6)	258(8)	F	0.62(3)	0.39(2)	0.64(3)	$E2/M1$	$19/2^-_1$	$17/2^-_1$
	2174.3(11)	97(3)	A	1.06(8)	1.19(8)	1.08(7)	$E2$	$19/2^-_1$	$15/2^-_2$
	2921.8(15)	5.0(4)					$E2$	$19/2^-_1$	$15/2^-_1$
5642.1(7)	2203.4(13)	4.4(7)					$(\Delta I=1)$	$(17/2_3)$[d]	$15/2^-_2$
	2949.9(21)	3.3(5)					$(\Delta I=1)$	$(17/2_3)$[d]	$15/2^-_1$
5771.1(17)	3207.8(18)	4.2(6)							$13/2^-_1$
5928.3(8)	2489.6(12)	2.6(3)							$13/2^-_2$
	3235.0(24)	1.6(3)							$11/2^-_2$
6092.1(11)	3401.5(17)	5.8(5)	A		1.19(29)		$(E2)$	$(19/2^-_2)$	$15/2^-_1$
6264.2(6)	622.1(3)	3.5(5)					$(\Delta I=1)$	$19/2^-_3$	$(17/2_3)$
	1881.1(9)	19(1)	D	0.98(16)	1.25(19)	1.02(17)	$E2/M1$	$19/2^-_3$	$17/2^-_1$

TABLE II. (*Continued.*)

E_x (keV)	E_γ (keV)	$I_{\rm rel}$ (%)	Gate[a]	$R_{\rm DCO}$ 150–127°	$R_{\rm DCO}$ 150–97°	$R_{\rm DCO}$ 127–97°	Mult. Ass.	I_i^π ($\hbar$)	I_f^π ($\hbar$)
	1954.2(10)	2.3(3)					$E2$	$19/2^-_3$	$15/2^-_3$
	3572.1(24)	6.7(8)	A		1.07(18)		$E2$	$19/2^-_3$	$15/2^-_1$
6297.2(7)	1914.2(9)	1.9(4)					$(\Delta I=1)$	$(19/2_4)$[d]	$17/2^-_1$
6457.7(8)	815.8(6)	2.2(3)					$(\Delta I=1)$	$19/2^-_5$	$(17/2_3)$
	2075.3(13)	12(1)	F		0.53(26)		$\Delta I=1$	$19/2^-_5$	$17/2^-_1$
	2147.8(17)	1.9(5)					$E2$	$19/2^-_5$	$15/2^-_3$
6533.2(6)	236.0(3)	1.3(2)					$(\Delta I=1)$	$21/2^-_1$	$(19/2_4)$
	269.0(2)	7.7(4)	A		0.63(16)		$E2/M1$	$21/2^-_1$	$19/2^-_3$
	919.9(5)	154(5)	B	0.52(3)	0.31(2)	0.56(3)	$E2/M1$	$21/2^-_1$	$19/2^-_1$
	2150.2(11)	389(12)	F	0.98(5)	1.09(5)	1.07(5)	$E2$	$21/2^-_1$	$17/2^-_1$
6654.3(7)	3962.8(26)	4.9(3)	A		0.65(16)		$\Delta I=1$	$17/2_4$	$15/2^-_1$
6682.8(7)	1583.6(8)	1.8(4)					$E2/M1$	$19/2^-_6$	$17/2^-_2$
	3243.7(24)	1.1(3)					$E2$	$19/2^-_6$	$15/2^-_2$
	3991.2(27)	3.1(5)	A		1.29(29)		$E2$[c]	$19/2^-_6$	$15/2^-_1$
6822.4(18)	4129.1(33)	3.1(3)	A		0.88(24)			17/2,19/2	$15/2^-_1$
7004.2(6)	471.0(2)	462(14)	D	0.77(3)	0.51(2)	0.77(3)	$E2/M1$	$23/2^-_1$	$21/2^-_1$
	739.7(5)	2.1(3)					$E2$	$23/2^-_1$	$19/2^-_3$
	1391.0(7)	85(3)	D	1.02(7)	1.10(7)	1.03(6)	$E2$	$23/2^-_1$	$19/2^-_1$
7017.2(6)	334.3(3)	3.4(3)	A		0.61(23)		$E2/M1$	$21/2^-_2$	$19/2^-_6$
	484.0(2)	11(1)	G		1.05(13)		$\Delta I=0$	$21/2^-_2$	$21/2^-_1$
	559.6(5)	1.4(2)					$E2/M1$	$21/2^-_2$	$19/2^-_5$
	1918.1(10)	47(3)	C		0.91(23)		$E2$	$21/2^-_2$	$17/2^-_2$
7224.1(7)	569.8(4)	1.1(2)					$\Delta I=1$	$19/2_7$	$17/2^-_4$
	1295.8(6)	3.6(8)						$19/2_7$	
	1581.8(7)	3.1(5)					$\Delta I=0$	$19/2_7$	$19/2^-_1$
	2125.9(11)	7.9(8)	H		0.68(21)		$\Delta I=1$	$19/2_7$	$17/2^-_2$
7315.4(8)	1701.6(9)	16(1)	D		0.62(16)		$E2/M1$[c]	$21/2^-_3$	$19/2^-_1$
7359.9(12)	706.1(9)	0.7(2)							$17/2_4$
	1588.6(12)	1.5(3)							
7405.5(7)	1141.4(6)	4.5(3)					$E2/M1$	$21/2^-_4$	$19/2^-_3$
	3022.8(15)	6.7(6)	F		0.99(14)		$E2$	$21/2^-_4$	$17/2^-_1$
7600.3(9)	1336.2(9)	3.0(4)					$(\Delta I=1)$	$(21/2_5)$	$19/2^-_3$
	1958.0(12)	1.5(5)					$(E2)$	$(21/2_5)$	$(17/2_3)$
	1987.2(14)	5.4(7)					$(\Delta I=1)$	$(21/2_5)$	$19/2^-_1$
7960.7(7)	956.5(5)	329(12)	D	0.84(4)	0.63(3)	0.79(3)	$E2/M1$	$25/2^-_1$	$23/2^-_1$
	1427.8(7)	28(2)	D		1.02(12)		$E2$	$25/2^-_1$	$21/2^-_1$
7978.8(8)	961.6(6)	19(1)	E		0.57(8)		$E2/M1$	$23/2^-_2$	$21/2^-_2$
	2365.6(12)	41(2)	D	1.10(10)	1.10(9)	0.96(8)	$E2$	$23/2^-_2$	$19/2^-_1$
8022.1(7)	797.6(7)	1.2(4)					$\Delta I=1$	$21/2_6$	$19/2_7$
	1017.8(5)	4.8(3)					$\Delta I=0$	$21/2_6$	$21/2^-_2$
	1198.9(17)	0.6(2)						$21/2_6$	17/2,19/2
	1367.9(7)	1.7(2)					$E2$	$21/2_6$	$17/2^-_4$
	1930.6(10)	1.4(5)					$\Delta I=1$	$21/2_6$	$19/2^-_2$
	2408.7(12)	17(1)	G		0.72(10)		$\Delta I=1$	$21/2_6$	$19/2^-_1$

TABLE II. (*Continued.*)

E_x (keV)	E_γ (keV)	$I_{\rm rel}$ (%)	Gate[a]	$R_{\rm DCO}$ 150–127°	$R_{\rm DCO}$ 150–97°	$R_{\rm DCO}$ 127–97°	Mult. Ass.	I_i^π ($\hbar$)	I_f^π ($\hbar$)
8237.1(7)	831.6(6)	2.6(3)					$E2/M1$	$23/2^-_3$	$21/2^-_4$
	1219.8(6)	12(1)	E		0.52(8)		$E2/M1$	$23/2^-_3$	$21/2^-_2$
	1780.0(11)	2.1(4)					$E2$	$23/2^-_3$	$19/2^-_5$
8451.8(8)	1046.4(5)	1.8(2)					$(E2/M1)$	$(23/2^-_4)$[d]	$21/2^-_4$
	1136.1(7)	3.8(7)					$(E2/M1)$	$(23/2^-_4)$[d]	$21/2^-_3$
	2188.1(14)	1.7(4)					$(E2)$	$(23/2^-_4)$[d]	$19/2^-_3$
8744.2(11)	1384.2(10)	1.9(5)						$23/2_5$	
	1740.0(9)	8.3(8)	D	1.07(19)	1.46(26)	1.22(25)	$\Delta I=0$	$23/2_5$	$23/2^-_1$
9034.0(7)	1011.9(5)	3.3(4)					$\Delta I=1$	$23/2_6$	$21/2_6$
	1810.3(9)	9.7(5)	I		1.01(19)		$E2$	$23/2_6$	$19/2_7$
	2016.6(10)	2.9(5)	E		0.52(13)		$\Delta I=1$	$23/2_6$	$21/2^-_2$
9401.8(8)	1422.9(7)	7.4(6)					$E2/M1$	$25/2^-_2$	$23/2^-_2$
	1996.6(11)	2.2(4)					$E2$	$25/2^-_2$	$21/2^-_4$
	2086.4(12)	2.5(4)					$E2$	$25/2^-_2$	$21/2^-_3$
	2397.4(12)	6.7(6)	G		0.47(11)		$E2/M1$	$25/2^-_2$	$23/2^-_1$
	2869.1(14)	6.3(5)	G		1.03(21)		$E2$	$25/2^-_2$	$21/2^-_1$
9580.2(8)	1343.0(8)	4.9(8)	A		0.50(11)		$E2/M1$	$25/2^-_3$	$23/2^-_3$
	1619.7(8)	5.5(4)	D		1.34(14)		$\Delta I=0$	$25/2^-_3$	$25/2^-_1$
	2562.7(13)	2.6(4)					$E2$	$25/2^-_3$	$21/2^-_2$
	2575.7(14)	5.2(7)	D		0.94(15)		$E2/M1$	$25/2^-_3$	$23/2^-_1$
10105.8(9)	1071.8(5)	3.7(5)	F		0.38(18)		$\Delta I=1$	$25/2_4$	$23/2_5$
	2083.6(12)	15(1)	D		1.08(27)		$E2$	$25/2_4$	$21/2_6$
10381.0(8)	800.8(4)	8.0(12)	D		0.54(14)		$E2/M1$	$27/2^-_1$	$25/2^-_3$
	2144.0(19)	0.5(3)					$E2$	$27/2^-_1$	$23/2^-_3$
	2420.3(12)	31(3)	G		0.81(27)		$E2/M1$	$27/2^-_1$	$25/2^-_1$
10412.9(13)	1668.7(8)	3.9(7)							$23/2_5$
10708.3(9)	1306.6(6)	2.3(3)					$E2/M1$	$27/2^-_2$	$25/2^-_3$
	2729.7(14)	5.6(5)					$E2$	$27/2^-_2$	$23/2^-_2$
	2746.9(14)	5.5(7)					$E2/M1$	$27/2^-_2$	$25/2^-_1$
	3704.6(19)	11(2)	D		1.22(19)		$E2$	$27/2^-_2$	$23/2^-_1$
11017.2(10)	3056.1(17)	1.5(4)					$E2/M1$	$27/2^-_3$	$25/2^-_1$
	4013.6(20)	8.1(6)	D		1.02(18)		$E2$	$27/2^-_3$	$23/2^-_1$
11264.4(10)	1158.7(9)	1.3(6)					$E2/M1$	$27/2_4$	$25/2_4$
	2230.3(11)	9.4(7)	H		0.93(13)		$E2$	$27/2_4$	$23/2_5$
11524.5(19)	3563.8(18)	3.4(6)							$25/2^-_1$
11704.8(14)	1291.8(7)	1.1(4)						$27/2_5$	
	3744.4(23)	3.6(5)	D		0.45(13)		$\Delta I=1$	$27/2_5$	$25/2^-_1$
11823.3(10)	806.1(4)	1.2(4)					$(E2/M1)$	$(29/2^-_1)$[d]	$27/2^-_3$
	2243.1(14)	4.2(7)					$(E2)$	$(29/2^-_1)$[d]	$25/2^-_3$
	2421.4(12)	10(1)					$(E2)$	$(29/2^-_1)$[d]	$25/2^-_2$
	3862.9(28)	1.7(4)					$(E2)$	$(29/2^-_1)$[d]	$25/2^-_1$
12067.7(21)	4107.1(26)	1.2(5)							$25/2^-_1$
12216.4(14)	2110.6(11)	4.7(8)					$(E2)$	$(29/2_2)$[d]	$25/2_4$
12466.6(12)	1449.4(8)	1.0(3)					$E2/M1$	$29/2^-_3$	$27/2^-_3$
	4505.4(23)	6.1(4)	D		0.95(15)		$E2$	$29/2^-_3$	$25/2^-_1$

TABLE II. (*Continued.*)

E_x (keV)	E_γ (keV)	$I_{\rm rel}$ (%)	Gate[a]	$R_{\rm DCO}$ 150–127°	$R_{\rm DCO}$ 150–97°	$R_{\rm DCO}$ 127–97°	Mult. Ass.	I_i^π ($\hbar$)	I_f^π ($\hbar$)
12816.5(21)	748.8(6)	0.6(3)							
	4855.7(28)	0.7(3)							$25/2^-{}_1$
13080.5(15)	2372.2(12)	4.3(6)							$27/2^-{}_2$
13175.6(14)	1911.2(10)	3.4(6)	I		0.93(23)		$(E2)$	$(31/2_1)$[d]	$27/2_1$
13809.4(14)	1342.8(7)	1.9(5)							$29/2^-{}_3$
14091.7(15)	1625.1(8)	1.1(4)							$29/2^-{}_3$

[a]A, 1441 and 1252 keV; B, 1441, 2150, and 2174 keV; C, 1675 keV; D, 1252, 1441, 2150, and 2174 keV; E, 1911/1918 keV (doublet); F, 1820 keV; G, 2150 and 2174 keV; H, 1810/1820 and 1911/1919 keV (doublets); I, 2230 keV.
[b]Adopted from Ref. [16].
[c]Assignment based (also) on DCO ratios of feeding transition(s).
[d]Tentative assignment based on yrast arguments.

1315 keV, which is shown on the right-hand side of the level scheme of ^{54}Fe in Fig. 1. The sequence is labeled D3. The spectrum in Fig. 4(a) is in coincidence with any of the three rather intense dipole transitions (cf. Table I), and a second coincidence with the 4017-keV, $11^-{}_1 \rightarrow 10^+{}_1$ yrast transition is required. This 4017-keV transition feeds the 6526-keV 10^+ isomer. The clean spectrum in Fig. 4(a) thus features all γ-ray decays *into* the D3 structure. As expected, transitions below the 10^+ isomer can hardly be seen in Fig. 4(a), e.g., those at 146 and marked at 411 keV.

The D3 sequence is found to connect to three previously unobserved structures at higher spins. The lines at 2206, 2924, 3087, and 3136 keV in Fig. 4(a) are the main connections toward the D4 dipole structure (see below), formed by the 881, 1153, 1196, and 1784 transitions, which are also clearly seen in this spectrum. Second, next to the 2924-keV connection toward D4, transitions at 2545, 2745, and 3945 keV are found to feed directly into the 13359-keV 14^- yrast state of D3. Third, the sequence of 673-2913-keV γ rays is found to connect the 12044-keV 13^- state in D3 with a 15631-keV 16^+ state, which belongs to the structure labeled Q1 in Fig. 1. This connection is highlighted in Fig. 4(c), which shows a

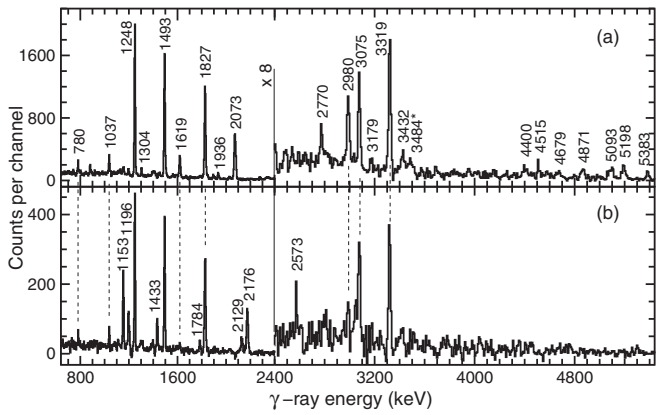

FIG. 3. γ-ray spectra related to the positive-parity yrast structure above the isomeric 6526-keV 10^+ state in ^{54}Fe (see Fig. 1). All spectra are selected for the analysis of ^{54}Fe residues according to the description in Sec. III. The spectra are in coincidence with any of the three 1493-, 1827-, or 1248-keV transitions and, in addition, the 1220-keV $14^+{}_1 \rightarrow 13^+{}_1$ transition [panel (a)] or the 1860-keV $14^+{}_2 \rightarrow 13^+{}_1$ transition [panel (b)]. Energy labels are in keV. An asterisk, $*$, indicates a transition, which could not be placed unambiguously in the ^{54}Fe level scheme. The binning is 4 keV (8 keV) per channel on the left-hand (right-hand) side of the spectra. Note the change of y scale at 2400 keV.

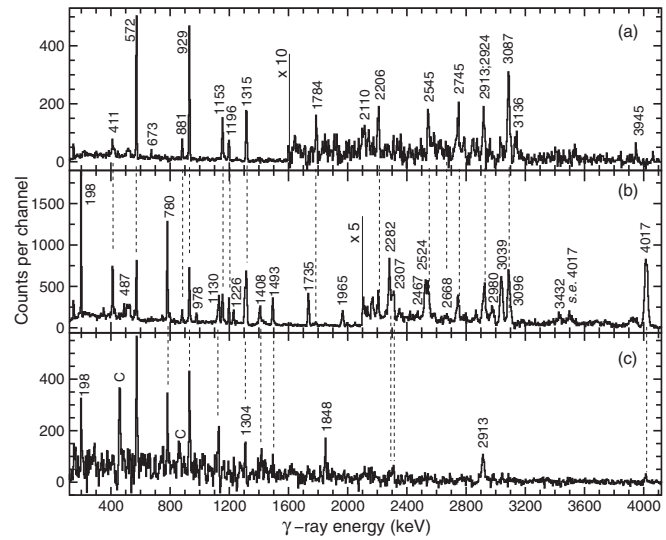

FIG. 4. γ-ray spectra related to the negative-parity yrast structure of ^{54}Fe shown on the right-hand side of Fig. 1. All spectra are selected for the analysis of ^{54}Fe residues according to the description in Sec. III. The spectrum in panel (a) is in coincidence with the 4017-keV $11^-{}_1 \rightarrow 10^+{}_1$ transition and any of the three subsequent intense $\Delta I = 1$ transitions at 572, 929, or 1315 keV. Panel (b) shows a spectrum of the sum of γ-ray coincidences with any pair of these three transitions. The spectrum in panel (c) is taken in coincidence with the 673-keV transition, which connects the energy levels at 15631 and 14958 keV. Energy labels are in keV. The letter C indicates a known contamination from other reaction channels. The binning is 4 keV per channel. Note the change of y scale in panels (a) and (b). The notation *s.e.* signals a single-escape peak.

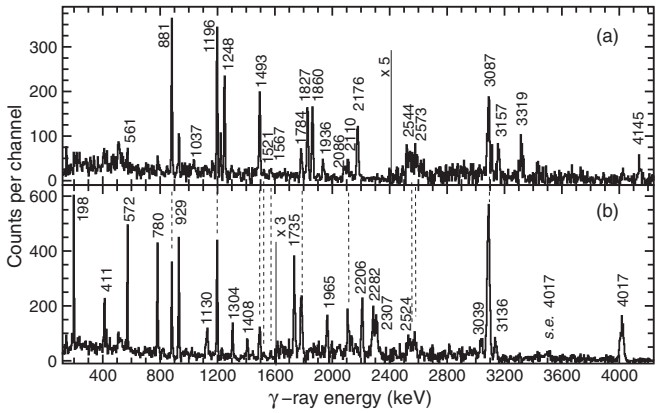

FIG. 5. γ-ray spectra related to a previously unobserved negative-parity dipole sequence in ^{54}Fe, shown at the top right of Fig. 1. All spectra are selected for the analysis of ^{54}Fe residues according to the description in Sec. III. Both spectra are in coincidence with the 1153-keV $16^-_1 \rightarrow 15^-_1$ transition. For the spectrum in panel (a), another coincidence with any of the three 1493-, 1827-, or 1248-keV transitions is required (cf. Fig. 3). For the spectrum in panel (b), another coincidence with any of the three 572-, 929-, or 1315-keV transitions is required (cf. Fig. 4). Energy labels are in keV. The binning is 4 keV per channel. Note the change of y scale in both panels. The notation *s.e.* signals a single-escape peak.

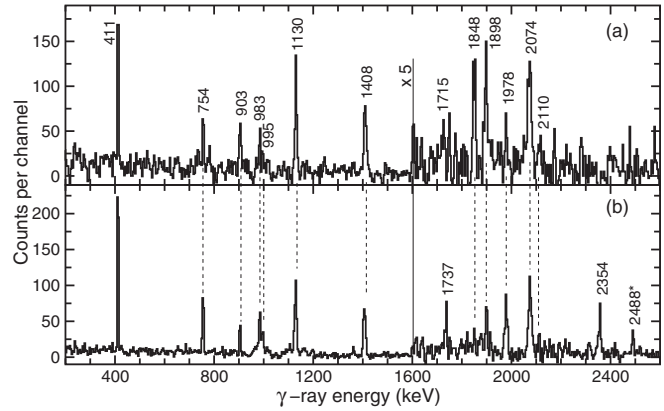

FIG. 6. γ-ray spectra related to the previously unobserved sequence in ^{54}Fe, shown on the left-hand side of Fig. 1. All spectra are selected for the analysis of ^{54}Fe residues according to the description in Sec. III. The spectrum in panel (a) is in coincidence with the 2354-keV $16^+_1 \rightarrow 14^+_3$ transition and any of the five transitions at 2074, 903, 995, 983, or 754 keV. The spectrum in panel (b) is in coincidence with the 4619-keV $8^+_5 \rightarrow 6^+_1$ transition and any of the four transitions at 754, 983, 995, or 903 keV. An asterisk, $*$, indicates a transition which could *not* be placed unambiguously in the ^{54}Fe level scheme. Energy labels are in keV. The binning is 4 keV per channel. Note the change of y scale at 1600 keV.

γ-ray spectrum in coincidence with the 673-keV transition: It reveals the 1848-keV line on top of the 16^+ state, the 2913-keV transition into the 12044-keV 13^- state, as well as the main transitions associated with the decay from D3 at, for instance, 198, 780, 1304, 2282, 2307, and 4017 keV. Because of low statistics and the doublet structure 2913/2924 keV, it is not possible to deduce DCO ratios to fix the spin and parity of the intermediate state at 14958 keV. Nevertheless, since spins and parities of initial and final states of the 673-2913-keV sequence are known, the 14958-keV state should represent either an $I^\pi = 14^+$ or 15^- level, respectively.

The spectrum in Fig. 4(b) is the sum of spectra in coincidence with any pair of three intense dipole transitions forming D3. Next to the transitions feeding into D3, it also reveals the many decay-out paths of D3: There are those ending in the 6526-keV 10^+ isomer at, e.g., 2307-2282 keV, 3039-780-198 keV, 3039-978 keV, 3096-1493 keV, or 4017 keV. There are also those bypassing the isomer, marked for instance by the presence of the 1965-1226-487-keV transitions.

The well-established DCO ratios of the three transitions at 572, 929, and 1315 keV and many of the main feeding and depopulating transitions provide unambiguous spin assignments to the levels of D3 and those connecting to it, including $I = 14$ and $I = 15$ to the 14250- and 15131-keV states in D4, respectively. Notably, both D3 and D4 structures must have the same parity. Since none of the (high-energy) dipole transitions connecting to known positive-parity states reveals significant quadrupole admixtures, which would be very likely for parity-conserving $E2/M1$ transitions, negative parity is assigned to both D3 and D4.

The γ-ray spectra in Fig. 5 focus on the dipole structure D4. Both spectra are taken in coincidence with the central 1153-keV $16^- \rightarrow 15^-$ transition. The spectrum in Fig. 5(a) demands a second coincidence with any of the 1493-, 1827-, or 1248-keV transitions. It thus highlights the decay path of D4 directly into the positive-parity yrast structure on top of the 6526-keV 10^+ isomer, namely via transitions at, for example, 1936, 2176, 3157, or 4145 keV. Correspondingly, the spectrum in Fig. 5(b) demands a second coincidence with any of the three main members of D3 (572, 929, or 1315 keV). Thus, this spectrum features the connections between D4 and D3 at 2206, 3087, and 3136 keV, the three transitions forming D3, as well as the decay sequences from D3 back into positive-parity yrast states [see discussion above and Fig. 4(b)].

Both spectra in Fig. 5 show intense peaks at 881, 1196, 1784, and 2110 keV, as well as weak ones at 561, 1521, and 1567 keV. The 881- and 561-keV lines form the lower part of D4. The decay of the 13689-keV state at the bottom of D4 is clearly fragmented. Only a transition at 2574 keV is found to directly connect into D3 (see also below). The 1196-2110- and 1784-1521-keV coincidences form parallel sequences toward the 19589-keV 18^- yrast state. The 1567-keV transition and one tentatively at 1908 keV are found or suggested to feed this state, reaching excited states beyond 21 MeV excitation energies. Note once more the presence (see also below) of the 1848-keV $17^- \rightarrow 16^+$ $E1$ connection between D4 and Q1. This transition provides both confidence in the level scheme and spin-parity assignment of the previously unobserved parts of the ^{54}Fe level scheme as a whole.

Finally, the spectra displayed in Fig. 6 focus on the newly established side structure labeled Q1 in Fig. 1. Experimentally, some low-spin members of Q1 at 6300, 7568, and 8322 keV were already proposed in Ref. [13]. The main link

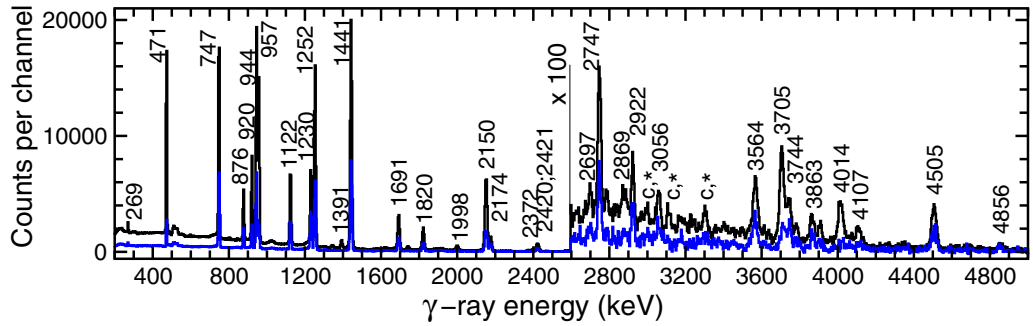

FIG. 7. γ-ray spectra focusing on the previously reported yrast structure in ^{53}Mn and new high-energy transitions. All spectra are selected for the analysis of ^{53}Mn residues according to the description in Sec. III. The spectrum in black is the sum of spectra taken in coincidence with the 957-, 471-, and 920-keV, $25/2^-_1 \rightarrow 19/2^-_1$ yrast cascade. The blue spectrum requires a second coincidence with any of these three transitions. To allow for a better comparison, the spectrum in black is suppressed by a factor of 5. The mark "c,*" indicates either a contaminating line or a transition which could *not* be placed unambiguously in the ^{53}Mn level scheme. Energy labels are in keV. The binning is 4 keV per channel. Note the considerable change of *y* scale at 2600 keV.

from Q1 back into the low-spin $6^+ \rightarrow 4^+ \rightarrow 2^+ \rightarrow 0^+$ yrast sequence is the 4619-keV $8^+_5 \rightarrow 6^+_1$ $E2$ transition. The γ-ray spectrum in Fig. 6(b) is in coincidence with this transition and any of the four 754-, 903-, 983-, and 995-keV $\Delta I = 1$ transitions placed on top of the 7568-keV 8^+_5 state. The spectrum shows the three peaks at 411, 1130, and 1408 keV, forming the mentioned low-spin $E2$ ground-state cascade, the four dipole transitions, and it reveals peaks at 1737, 1898, 1978, 2074, 2354, and 2488 keV. The former three mark crossover $E2$ transitions parallel to the 754-983-, 995-903-, and 983-995-keV dipole sequences, respectively. The 2074- and 2354-keV $E2$ transitions are placed on top of the 11 203-keV 12^+_3 state and reach the 15631-keV 16^+_1 yrast state mentioned earlier. The 2488-keV line could not be placed unambiguously into the level scheme due to its low yield, but it fits energetically between the lowest state in structure D4 at 13689 keV and the 11203-keV 12^+_3 state in Q1. The spin-parity assignments for this main sequence within the Q1 structure are given by the DCO ratios of the 2074-, 2354-, and 4619-keV (all stretched quadrupole) as well as the 754-, 903-, 983-, and 995-keV (all stretched dipole) transitions. The assignments are also consistent with the observation of a number of other transitions, which connect Q1 with other known positive-parity states; the transitions at 2395, 2924, 4677, 2625, or 3147 keV (cf. Fig. 1) have implied stretched $E2$ character.

The spectrum in Fig. 6(a) is in coincidence with the 2354-keV $16^+_1 \rightarrow 14^+_3$ transition and the 2074-keV $14^+_3 \rightarrow 12^+_3$ $E2$ transition or any of the four dipole transitions in Q1 mentioned above. Here, the 1848-keV connection toward the D4 cascade is obvious, and even the 2110-keV line belonging to D4 is weakly present in that spectrum. Because of the 2074-2354-keV coincidence, Fig. 6(b) reveals also a weak 1715-keV line, which is part of another, Q1-related parallel side structure. Despite the lack of DCO ratios, firm spin-parity assignments to the levels at 5482, 5884, 7254, 7753, 8130, and 9487 keV can be performed, because there are limited numbers of transitions connecting states with known spin and parities. To exemplify the procedure, the four γ rays with energies 1715, 1356, 2246, and 3347, placed at the very left-hand side of the level scheme in Fig. 1, connect the 11203-keV 12^+_3 state with the 2537-keV 4^+_1 yrast state. In prompt γ-ray spectroscopy, the total spin difference of $\Delta I = 8$ between these two levels implies four transitions with stretched $E2$ character in between, providing a firm 10^+, 8^+, and 6^+ assignment to the states at 9487, 8130, and 5884 keV, respectively.

B. The ^{53}Mn level scheme

The low- to medium-spin yrast sequence of ^{53}Mn was established by Lister *et al.* [15]. This comprises the intense γ-ray transitions toward the right-hand side of Fig. 2, reaching the $25/2^-$ state at 7961 keV. A few other states were previously observed by α-particle-induced reactions [16], for instance, the yrare $11/2^-$ and $13/2^-$ states at 2697 and 3424 keV, respectively.

The spectrum in black in Fig. 7 shows the sum of spectra in coincidence with the three known dipole transitions in the $25/2^- \rightarrow 23/2^- \rightarrow 21/2^- \rightarrow 19/2^-$ yrast cascade, located at 957, 471, and 920 keV, respectively. The spectrum in blue is the sum of the three spectra in mutual coincidence with two of these three transitions. A few, possibly contaminating coincidence peaks at high γ-ray energy disappear in the latter, while already the spectrum in black is essentially contaminant free, not the least due to the highly selective charged-particle requirement. Besides the main and known cascade down to the ground state of ^{53}Mn, i.e., the transitions at 471, 747, 876, 920, 957, 1122, 1230, 1252, 1391, 1441, 1691, 1820, 2150, and 2174 keV, the spectrum reveals two weak lines at 1998 keV, $15/2^-_2 \rightarrow 11/2^-_1$, and 2922 keV, $19/2^-_1 \rightarrow 15/2^-_1$, complementing the yrast structure. One low-energy transition is observed at 269 keV ($21/2^-_1 \rightarrow 19/2^-_3$, see below), but most striking is the large number of hitherto unobserved lines in the high-energy regime between 2.4 and 5.0 MeV γ-ray energy. Following an in-depth analysis, the majority of these high-energy transitions is found to directly feed the 7961-keV $25/2^-$ yrast state. The yield of some of them allows the extraction of DCO ratios. Furthermore, most of the newly observed high-spin states are connected by more than one cascade: For instance, the 9402-keV $25/2^-_3$ level decays via the 2869-keV $E2$ transition into the $21/2^-_1$ state, the 2397-keV $E2/M1$

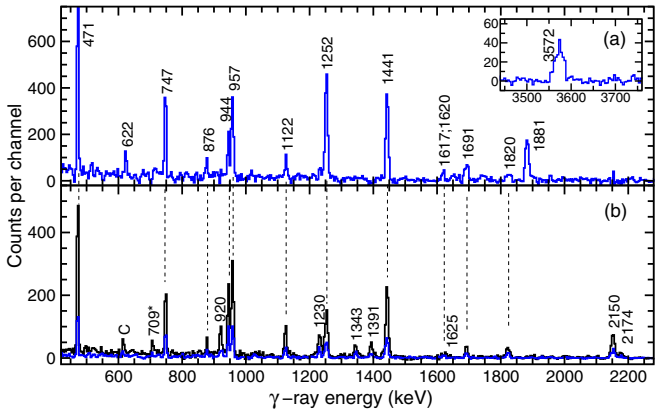

FIG. 8. γ-ray spectra related to newly observed parts of the ^{53}Mn level scheme (cf. Fig. 2). All spectra are selected for the analysis of ^{53}Mn residues according to the description in Sec. III. The blue spectrum in panel (a) is in coincidence with the previously unobserved 269-keV $21/2^-_1 \rightarrow 19/2^-_3$ transition and any of the intense yrast transtions at 471, 957, 1122, 1252, or 1441 keV. The spectra in panel (b) are in coincidence with the high-energy transition at 4505 keV, feeding the 7961-keV $25/2^-$ yrast state. For the blue spectrum, an additional coincidence with any of the intense yrast transtions at 471, 920, 957, 1122, 1252, or 1441 keV is demanded. An asterisk, $*$, indicates a transition which could *not* be placed unambiguously in the ^{53}Mn level scheme. The letter C indicates a known contamination from another reaction channel. Energy labels are in keV. The binning is 4 keV per channel.

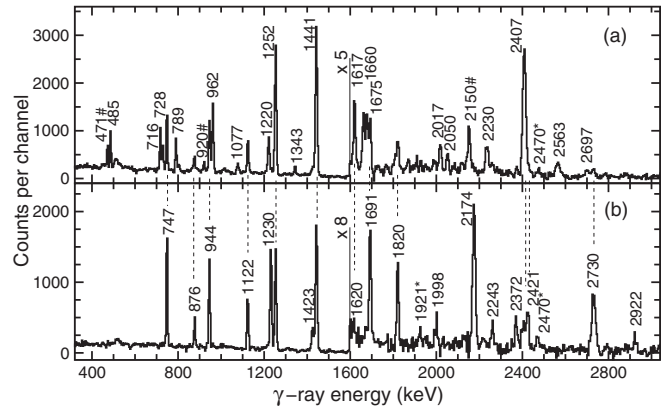

FIG. 9. γ-ray spectra related to the central part of the ^{53}Mn level scheme (cf. Fig. 2). All spectra are selected for the analysis of ^{53}Mn residues according to the description in Sec. III. The spectrum in panel (a) is in coincidence with the 1918-keV $21/2^-_2 \rightarrow 17/2^-_2$ transition, including some yield from the less intense 1921-keV transition, which connects $15/2^-$ states at 4614 and 2692 keV. A hashtag, #, indicates a line, which arises from coincidences with yet another but unplaced transition of similar energy from ^{53}Mn. The spectrum in panel (b) is in coincidence with the 2366-keV $23/2^-_2 \rightarrow 19/2^-_1$ transition. An asterisk, $*$, indicates a transition which could *not* be placed unambiguously in the ^{53}Mn level scheme. Energy labels are in keV. The binning is 4 keV per channel. Note the change of y scale at 1600 keV.

transition into the $23/2^-_1$ state, and the 1423-keV transition into the 7979-keV $23/2^-_2$ state. Another example is the 11017-keV $27/2^-_3$ level, connecting via 3056- and 4014-keV transitions down to both the yrast $23/2^-$ and $25/2^-$ states. Via a 1449-keV transition, the $29/2^-_3$ state is reached, which is defined by the 4505-keV stretched $E2$ back into the 7961-keV $25/2^-$ yrast state. Similarly, the observation of states such as the 27/2 level at 11705 keV or the tentative $29/2^-$ level at 11 823 keV provides confidence to this observed network at high excitation energy and high spin in ^{53}Mn. The multitude of level connectivity puts also constraints on possible spins and parities of the involved states, in combination with a few DCO ratios as well as yrast, i.e., γ-ray intensity arguments.

The spectrum in Fig. 8(a) is in coincidence with the hitherto unobserved low-energy 269-keV transition, which connects the yrast $21/2^-$ state at 6533 keV with the $19/2^-_3$ level at 6264 keV and the intense yrast transitions at 471, 957, 1122, 1252, and 1441 keV. The spectrum exemplifies the quality of the $\gamma\gamma\gamma$ data for transitions with less than 1% relative yield: Coincidences with transitions at 622, 1881, and 3572 keV, decaying from the $19/2^-_3$ level, are apparent, and the DCO ratio of the 269-keV transition points to a stretched dipole, which in connection with the existence of the 3572-keV coincidence and its DCO ratio determines the spin and parity of the 6264-keV state to $19/2^-$. The other peaks seen in Fig. 8(a) correspond to the transitions expected from various decay sequences toward the ground state, as well as the intense 471- and 957-keV transitions feeding the 6533-keV state. Similarly, the spectra in Fig. 8(b) illustrate the possibilities to establish high-energy transitions, in this case the previously unobserved 4505-keV line feeding into the $25/2^-$ yrast state at 7961 keV. The black spectrum in Fig. 8(b) is taken in coincidence with the 4505-keV transition, while the blue spectrum in Fig. 8(b) requires an additional coincidence with intense yrast transitions at 471, 957, 1122, 1252, and 1441 keV, which acts as additional filter for ^{53}Mn. While the yield is reduced by about a factor of 3 due to the additional coincidence requirement, minor contaminations can be removed, while both spectra clearly point to an unambiguous placement of the 4505-keV transition. Also in this case it is possible to deduce a DCO ratio, which in connection with yrast arguments yields a spin-parity assignment of $29/2^-$ to the state at 12467 keV, also evidenced by the parallel 1449-4014-keV sequence into the yrast $23/2^-$ level at 7004 keV.

The yrare part of the ^{53}Mn level scheme toward the center of Fig. 2 is subject of the two exemplifying spectra displayed in Fig. 9. The spectrum in Fig. 9(b) is in coincidence with the 2366-keV $23/2^-_2 \rightarrow 19/2^-_1$ $E2$ transition. It reveals the above-mentioned yrast cascade down to the ground state, including the newly established weak 1998- and 2922-keV transitions. The 2730-keV coincidence connects to the previously mentioned yrare $27/2^-$ state at 10708 keV, with the 2372-keV transition on top. The 1423-keV line depopulates the previously mentioned $25/2^-_3$ state at 9402 keV, with the 2421-keV transition connecting further to the 11823 level, which is also reached via the parallel 1620-2243-keV cascade. Weak transitions at 1921 and 2470 keV could not be placed in the ^{53}Mn

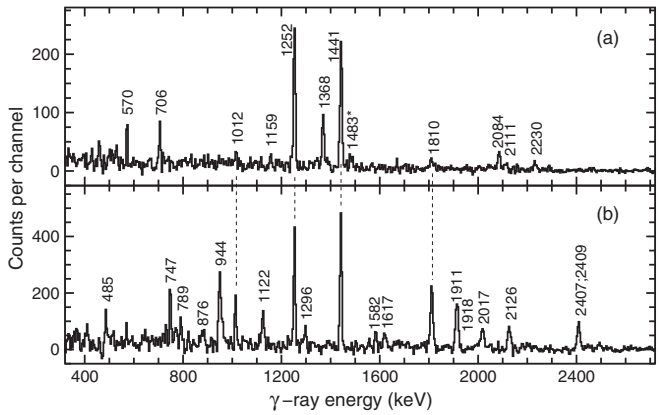

FIG. 10. γ-ray spectra related to the previously unobserved sequence in ^{53}Mn, shown on the left-hand side of Fig. 2. All spectra are selected for the analysis of ^{53}Mn residues according to the description in Sec. III. The spectrum in panel (a) is in coincidence with the 3963-keV transition, which connects the 17/2 state at 6654 keV with the $15/2^-$ yrast level. The spectrum in panel (b) is in coincidence with the 2230-keV $27/2 \rightarrow 23/2$ transition. An asterisk, $*$, indicates a transition which could *not* be placed unambiguously in the ^{53}Mn level scheme. Energy labels are in keV. The binning is 4 keV per channel.

level scheme. The spectrum in Fig. 9(a) is in coincidence with the central 1918-keV $21/2^-_2 \rightarrow 17/2^-_2$ transition. It includes some yield from the less intense 1921-keV doublet, which connects $15/2^-$ states at 4614 and 2692 keV. The weak presence of lines at 471, 920, and 2150 keV, which belong to the known yrast sequence in ^{53}Mn, indicates the presence of another transition at a γ-ray energy close to 1920 keV at higher excitation energy (see above), which could not be unambiguously placed in the level scheme. Transitions labeled at 485, 716, 728, 747, 789, 876, 944, 1077, 1122, 1252, 1441, 1617, 1660, 1675, 1691, 1820, 2050, 2407, and 2697 keV can be identified in one of the decay paths of the 5099-keV, yrare $17/2^-_2$ level. The relatively intense 962-keV transition connects to the 7979-keV $23/2^-_2$ state mentioned earlier. The 2563-keV $E2$ as well as the parallel 1220-1343-keV sequence are clearly observed in Fig. 9(a) as well. The spectrum also reveals a connection into the structure marked Q1 on the left-hand side of Fig. 2: The 2230-keV $E2$ is visible, populating the 7017-keV yrare $21/2^-$ level via the line observed at 2017 keV. The weak transition observed at 2470 keV may possibly be positioned on top of either the 10381- or 11823-keV states. Once again, based on several DCO ratios of the more intense γ-ray transitions, the multitude of parallel sequences in this central nonyrast section of the level scheme of ^{53}Mn allows for (tentative) spin-parity assignments for most of the observed states.

Finally, the spectra shown in Fig. 10 focus on the identification of the structure labeled Q1 in Fig. 2. Figure 10(a) is taken in coincidence with the stretched dipole 3963-keV transition, linking the 17/2 state at 6654 keV directly to the yrast $15/2^-$ state at 2692 keV. Consequently, the spectrum is dominated by the 1252-1441-keV cascade toward the ground state of ^{53}Mn. The transitions seen at 570 and 1368 keV are part of Q1 and found to populate the 6654-keV level, while the 706-keV transition connects to the structure on the very right-hand side of Fig. 2. The remaining weak transitions labeled in Fig. 10(a), at 1012 and 1159, as well as 1810, 2084, 2111, and 2230 keV, are found to be (tentative) dipole and quadrupole members of a coupled bandlike structure concluding in a tentative 31/2 level at 13176 keV. Next to the 3963-keV transition, there are a number of (high-energy) transitions linking Q1 with the negative-parity yrast and yrare sequences of the comprehensive level scheme of ^{53}Mn. DCO ratios can be derived for several transitions toward Q1 and inside Q1, which yield firm spin assignments of its low-spin members. However, none of them allows us to unambiguously determine the parity of Q1. Figure 10(b) is a spectrum in coincidence with the 2230-keV in-band transition, which was already mentioned in the previous paragraph. The other quadrupole transitions in Q1 at 1296, 1810, and 1911 keV are clearly visible, as is the 1012-keV line connecting to the other signature of Q1. Transitions at 1582, 2017, 2126, and 2409 keV are examples of linking transitions. The presence of transitions at 485, 789, 1617, 1918, and 2407 keV indicate that a sizable part of the yield of Q1 proceeds via the yrare $17/2^-_2$ level at 5099 keV. Peaks at 747, 876, 944, 1122, 1252, and 1441 keV belong to the known low-spin regime of the yrast sequence of ^{53}Mn. The relative yield of the "Q1 band" is on the order of 1 to 2% of the full population of ^{53}Mn.

V. DISCUSSION

Since ^{53}Mn and ^{54}Fe are semimagic $N = 28$ isotones, large-scale shell-model calculations are called for to interpret the largely irregular patterns of the level schemes shown in Figs. 1 and 2. For ^{54}Fe, see also the previous case study in Ref. [13]. Already then the structure labeled D3 in Fig. 1 was observed but could *not* be explained with shell-model calculations within the full fp model space. This indicates the need to excite of at least one proton or neutron into the positive-parity $1g_{9/2}$ intruder orbital. Therefore, cranked Nilsson-Strutinsky calculations were performed to study these seemingly more collective "band" structures in ^{54}Fe (D3, D4, Q1) and ^{53}Mn (Q1) in some more detail.

A. Shell-model calculations

Employing the shell-model code ANTOINE [28,29], the calculations comprise the full fp space including the $1f_{7/2}$ orbital below and the $2p_{3/2}$, $1f_{5/2}$, and $2p_{1/2}$ orbitals above the $N, Z = 28$ shell closure. The configuration space was truncated to allow for the excitation of up to seven particles from the $1f_{7/2}$ shell into the upper fp shell, for which the notation $t = 7$ is used. Calculations performed on yrast structures in $A = 50$, $A = 51$, and $A = 52$ have shown that results from calculations with this truncation are essentially indistinguishable from calculations performed in the full fp configuration space [30], compromising between computational efforts and sufficient convergence for the calculated numbers (see also, e.g., Refs. [31–33]). Notably, a rotational band in doubly-magic ^{56}Ni can be reproduced by shell-model calculations with a $t = 6$ truncation scheme [2].

TABLE III. Numerical assessments of the level of agreement between matched observed and calculated shell-model states in ^{54}Fe and ^{53}Mn by means of mean level deviations (MLD), binding energy shifts (BES), and mean branching deviation (MBD) [36]. For a given isotope and shell-model parameterization, results are provided for strongly populated, mainly yrast states (y), then adding more yrare states into the picture (yy), and finally for all states (a) that allow a mapping between experiment and theory. See Tables IV and VI for details. The number of states considered is given in parantheses, (n_1, n_2), with n_1 being the number of states used for MLD and BES and n_2 for MBD, respectively.

Nucleus	Shell-model interaction	States	MLD (keV)	BES (keV)	MBD
^{54}Fe	KB3G[a]	y (16,11)	260	−253	0.034
		yy (30,24)	229	−282	0.047
		a (40,34)	223	−317	0.050
	+ISB[a]	y (16,11)	238	−100	0.026
		yy (30,24)	218	−123	0.044
		a (40,34)	211	−135	0.048
	GXPF1A	y (16,11)	241	361	0.148
		yy (30,24)	247	353	0.093
		a (40,34)	227	331	0.092
^{53}Mn	KB3G[b]	y (11,8)	76	−165	0.007
		yy (29,26)	173	−140	0.080
		a (42,39)	185	−184	0.081
	+ISB[b]	y (11,8)	39	−84	0.010
		yy (29,26)	159	−19	0.072
		a (42,39)	163	−50	0.079
	GXPF1A	y (11,8)	195	223	0.023
		yy (29,26)	192	295	0.066
		a (42,39)	171	294	0.078

[a]Predicted 4^+_3 and 4^+_4 as well as 12^+_1 and 12^+_2 states exchanged. See text for details.

[b]Predicted $21/2^-_4$ and $21/2^-_5$ states exchanged. See text for details.

For the study of ^{53}Mn and ^{54}Fe, two interactions have been studied, namely the standard GXPF1A [34] and KB3G [30] interactions. To probe the influence of isospin breaking (ISB) effects, a calculation based on KB3G but modified according to the prescription of Ref. [32] has been performed as well. To probe decay patterns, all calculations are using bare g factors and effective nucleon charges taken from Ref. [35], i.e., $\varepsilon_p = 1.15e$ and $\varepsilon_n = 0.80e$ for protons and neutrons, respectively. The experimental γ-ray energies were used to compute transition strengths and deduce branching ratios and mixing ratios of the transitions and lifetimes of the nuclear states.

The association of observed and calculated levels starts from the predicted sequence of states for a given spin value. There are, however, a few cases of subsequent states lying close in energy, for which an exchange yields considerably improved descriptions of both their feeding and decay patterns. In these cases, the decay pattern is the leading argument for the association of observed and calculated levels. Once the association is settled, mean level deviations (MLD) in conjunction with binding energy shifts (BES) provide an overview of the agreement between experiment and theory in terms of energetics. To better estimate the quality of the predicted wave functions, one can compare the electromagnetic properties, which manifests in typically a few lifetimes and transition strengths, but also in many observed and calculated branching ratios for the states. They can be assessed by means of mean branching deviations (MBD) [36]. The numerical results for these quantities are summarized in Table III.

Overall, the KB3G+ISB parameterization provides the best agreement between experiment and theory. While the quality of predicted electromagnetic decay properties is similar for KB3G+ISB and plain KB3G for the respective sets of states in ^{54}Fe and ^{53}Mn, the inclusion of the isospin breaking terms provides a significant improvement in terms of MLD and BES values. GXPF1A calls for large positive BES, opposite to similarly large negative BES for KB3G, but yields slightly worse MLD values than KB3G in most cases. Especially the decay pattern (MBD) of the yrast states are significantly less well described by the GXPF1A parameterization compared with KB3G or KB3G+ISB.

1. Notes on ^{54}Fe

The present shell-model study of ^{54}Fe is an extension of the one presented in Ref. [13]. The computational complexity increased due to the more comprehensive level scheme. Table IV provides a comparison of the measured branching ratios and the predictions of the three sets of shell-model calculations. This concerns all states with known spin-parity assignments for which a predicted state could be identified or suggested to match an observed one. Table V provides an overview of measured lifetimes and those predicted for a selection of yrast and yrare states in ^{54}Fe.

The yrast $E2$ cascade connecting the 6526-keV 10^+ isomer with the ground state is very well described by all parameterizations. This is manifested by the corresponding lifetime predictions, which lie within some ±30% of the experimental values, and often much better. The predicted essentially exclusive yrast $8^+ \rightarrow 6^+$ $E2$ decay is also in line with the observations. For a more detailed discussion of the $10^+ \rightarrow 6^+$ $E4$ branch, see Ref. [37].

The main ingredients of the nonyrast low-spin sequence, up to some 6 MeV excitation energy and including states not observed in the present work (0^+_2, 2^+_2, 2^+_3, 4^+_3, 3^+_2), are also caught by the calculations. For the KB3G interactions, an exchange of the predicted 4^+_3 and 4^+_4 states provides a much improved description of the feeding *and* decay pattern of the experimental states at 3833 and 4048 keV, respectively, seen in considerably improved MBD values for both states. Note that the 3833-keV state was not observed in the present study; it is known from earlier low-spin studies [14]. The change of the 4^+_3 and 4^+_4 states implies only a minor cost of the MLD. While the lifetime predictions for the 2^+_2 and 2^+_3 states may call for such an exchange as well, the branching ratios of these two states are in very good agreement with experiment. Thus, in terms of MLD and MBD measures, these states are kept in order. Except for the 4^+_4 state in the GXPF1A model, there is hardly any major notable discrepancy in that part of the level scheme, reaching the 5280-keV 6^+_3 and 5928 keV 7^+_1 states.

TABLE IV. Selection of experimental (Table I and Ref. [14]) and predicted branching ratios of excited states in ^{54}Fe. Energies of unobserved (n.o.) γ-ray transitions are listed in italic characters. Spin-parity labels in square brackets, $[I_i^\pi]$, represent suggested theoretical assignments. The column labeled "set" refers to the classification of states used for MLD, BES, and MBD assessments (cf. Table III).

E_x (keV)	set[a]	E_γ (keV)	I_i^π ($\hbar$)	I_f^π ($\hbar$)	$b_{\rm exp}$	KB3G	+ISB	GXPF1A
2959[b]	yy	2959	2^+_2	0^+_1	55(3)	53	49	75
		1551		2^+_1	45(3)	46	51	25
		421		4^+_1	n.o.	0	0	0
		398		0^+_2	n.o.	0	0	0
3166[b]	a	3166	2^+_3	0^+_1	81(3)	94	94	85
		1758		2^+_1	19(3)	6	6	15
		628		4^+_1	n.o.	0	0	0
		605		0^+_2	n.o.	0	0	0
3294	yy	1887	4^+_2	2^+_1	18(3)	6	8	8
		757		4^+_1	82(3)	94	92	92
		346		6^+_1	n.o.	0	0	0
		336		2^+_2	n.o.	0	0	0
		129		2^+_3	n.o.	0	0	0
3344	y	1937	3^+_1	2^+_1	56(2)	77	76	82
		807		4^+_1	44(2)	22	22	17
		386		2^+_2	n.o.	0	0	1
		179		2^+_3	n.o.	0	1	0
		50		4^+_2	n.o.	1	1	1
3833[b]	a	2425	4^+_3	2^+_1	89(3)	94	95	56
		1295		4^+_1	9(3)	1	0	5
		884		6^+_1	n.o.	0	0	0
		874		2^+_2	n.o.	5	4	2
		538		4^+_2	2(1)	1	1	19
		488		3^+_1	n.o.	0	0	18
4031	y	1494	5^+_1	4^+_1	14(3)	6	6	17
		1082		6^+_1	n.o.	6	7	2
		737		4^+_2	86(3)	89	88	80
		686		3^+_1	n.o.	0	0	0
		198		4^+_3	n.o.	0	0	1
4048	a	2640	4^+_4	2^+_1	24(12)	4	19	68
		1510		4^+_1	11(6)	38	34	19
		1099		6^+_1	n.o.	0	0	0
		1089		2^+_2	n.o.	0	2	6
		753		4^+_2	n.o.	4	3	0
		704		3^+_1	65(14)	54	42	7
		590		2^+_3	n.o.	0	0	0
4072[b]	yy	2664	3^+_2	2^+_1	93(1)	96	96	93
		1534		4^+_1	7(1)	1	1	3
4656	yy	*2118*	5^+_2	4^+_1	n.o.	11	12	17
		1707		6^+_1	n.o.	1	0	2
		1360		4^+_2	82(6)	72	71	62
		823		4^+_3	n.o.	7	9	6
		625		5^+_1	n.o.	2	2	0
		608		4^+_4	17(6)	3	2	5
5046	yy	*2508*	6^+_2	4^+_1	n.o.	0	0	0
		2097		6^+_1	81(3)	84	84	71
		1751		4^+_2	n.o.	0	0	3
		1213		4^+_3	n.o.	0	0	0
		1014		5^+_1	19(3)	15	15	26
		998		4^+_4	n.o.	0	0	0
5280	a	*2742*	6^+_3	4^+_1	n.o.	0	0	2
		2332		6^+_1	19(5)	4	5	22
		1985		4^+_2	22(6)	18	19	20
		1447		4^+_3	n.o.	0	0	37
		1249		5^+_1	49(8)	70	68	3
		1232		4^+_4	n.o.	1	1	2
		624		5^+_2	9(4)	7	7	14
5482	a	2945	6^+_4	4^+_1	88(5)	30	34	63
		2533		6^+_1	n.o.	2	2	10
		2187		4^+_2	n.o.	0	0	0
		1649		4^+_3	n.o.	67	62	16
		1434		4^+_4	12(5)	0	1	9
5884		3347	6^+_5	4^+_1	100	0	0	46
5928	y	2980	7^+_1	6^+_1	75(3)	45	49	61
		1897		5^+_1	6(2)	11	10	6
		1272		5^+_2	n.o.	0	0	0
		882		6^+_2	19(2)	41	38	32
		648		6^+_3	n.o.	3	3	0
6300	yy	3351	7^+_2	6^+_1	83(5)	18	52	91
		2269		5^+_1	n.o.	1	0	3
		1644		5^+_2	n.o.	16	11	0
		1254		6^+_2	17(5)	5	8	4
		1020		6^+_3	n.o.	48	21	0
6380	y	3432	8^+_1	6^+_1	100	97	98	99
6551	a	3602	7^+_3	6^+_1	49(7)	88	83	91
		2520		5^+_1	n.o.	3	0	2
		1895		5^+_2	n.o.	0	4	1
		1505		6^+_2	n.o.	4	5	2
		1270		6^+_3	40(7)	1	4	3
		1069		6^+_4	11(4)	0	0	1
		623		7^+_1	n.o.	4	4	0
6724	y	796	9^+_1	7^+_1	12(1)	5	6	32
		344		8^+_1	0(1)	16	15	0
		198		10^+_1	88(2)	80	80	68
6865	yy	3916	8^+_2	6^+_1	36(3)	47	52	57
		1819		6^+_2	8(2)	5	5	5
		1585		6^+_3	n.o.	0	0	2
		937		7^+_1	53(4)	46	42	33
		484		8^+_1	4(1)	1	1	3
7076	a	4127	8^+_3	6^+_1	44(13)	91	92	66
		1149		7^+_1	37(13)	3	4	24
		776		7^+_2	19(9)	2	1	4
7254	a	4305	8^+_4	6^+_1	60(5)	80	75	44
		2208		6^+_2	n.o.	0	0	19
		1974		6^+_3	n.o.	8	10	14
		1773		6^+_4	40(5)	7	11	14
		1326		7^+_1	n.o.	3	2	5
7352	yy	1424	9^+_2	7^+_1	40(3)	8	9	16
		972		8^+_1	10(2)	58	54	1
		826		10^+_1	n.o.	24	24	35
		628		9^+_1	n.o.	1	0	16
		487		8^+_2	50(3)	8	11	31
7504	yy	*1124*	10^+_2	8^+_1	n.o.	0	0	1
		978		10^+_1	10(1)	9	9	8
		780		9^+_1	90(1)	91	91	91
7568		4619	8^+_5	6^+_1	100	10	15	12

TABLE IV. (*Continued.*)

E_x (keV)	set[a]	E_γ (keV)	I_i^π ($\hbar$)	I_f^π ($\hbar$)	$b_{\rm exp}$	KB3G	+ISB	GXPF1A
7753		4804	8^+_6	6^+_1	100	15	12	24
8019	y	1493	11^+_1	10^+_1	100	100	100	99
8375	a	1995	10^+_3	8^+_1	100	36	37	9
8578	a	*2198*	10^+_4	8^+_1	n.o.	4	4	27
		2052		10^+_1	24(3)	39	40	32
		1854		9^+_1	n.o.	1	0	0
		1226		9^+_2	57(3)	43	42	33
		559		11^+_1	19(2)	11	10	4
8808	yy	2282	11^+_2	10^+_1	37(2)	2	1	3
		1304		10^+_2	59(2)	88	88	85
		789		11^+_1	4(1)	10	11	11
9123		1771	$[10^+_5]$	9^+_2	100	59	54	14
9846	y	3319	12^+_1	10^+_1	24(2)	75	74	32
		2342		10^+_2	2(1)	0	1	3
		1826		11^+_1	64(2)	22	24	52
		1471		10^+_3	n.o.	0	0	0
		1037		11^+_2	11(1)	2	2	3
		723		11^+_3	n.o.	0	0	11
10131	yy	*3605*	12^+_2	10^+_1	n.o.	6	5	21
		2627		10^+_2	n.o.	1	1	3
		2112		11^+_1	67(3)	64	69	62
		1756		10^+_3	n.o.	2	1	0
		1322		11^+_2	33(3)	27	23	13
11093	y	3075	13^+_1	11^+_1	13(1)	12	13	32
		2285		11^+_2	n.o.	0	0	0
		1247		12^+_1	87(1)	85	84	67
		962		12^+_2	n.o.	3	3	0
12314	y	2468	14^+_1	12^+_1	2(1)	4	3	62
		2182		12^+_2	1(1)	0	0	20
		1220		13^+_1	97(1)	95	96	16
		1111		12^+_3	n.o.	1	1	2
12954	yy	3108	14^+_2	12^+_1	9(1)	7	8	4
		2823		12^+_2	n.o.	0	0	0
		1860		13^+_1	91(1)	93	92	95
14386	y	3293	15^+_1	13^+_1	6(1)	2	2	12
		2073		14^+_1	80(2)	67	75	1
		1433		14^+_2	14(1)	31	23	87
15083	yy	*3990*	15^+_2	13^+_1	n.o.	0	0	14
		2770		14^+_1	48(4)	72	79	69
		2129		14^+_2	52(4)	4	2	13
15631			16^+_1			unmatched		
16005	y	3692	16^+_2	14^+_1	7(2)	16	13	39
		3052		14^+_2	11(3)	4	5	0
		2728		14^+_3	n.o.	5	4	2
		1619		15^+_1	82(5)	73	76	50
		922		15^+_2	n.o.	0	0	4
18901		4515	$[17^+_1]$	15^+_1	100	71	47	42

[a]y: yrast structure; yy: plus yrare states; a: all mapped states.
[b]Not observed in the present experiment.

The central part of the ^{54}Fe level scheme in Fig. 1, between some 7 and 16 MeV excitation energy, concerns yrast and yrare states in the spin-parity range 8^+–16^+. Many of the observed states are equally well described by the different parameterizations. Examples are the 6865-keV 8^+_2, the 7504-keV 10^+_2, the 8019-keV 11^+_1, the 11093-keV 13^+_1, and the 12954-keV 14^+_2 states. This yields confidence in the applicability of the shell-model approach. Starting with the yrast and yrare 9^+_1 and 9^+_2 states, respectively, some deviations between experiment and theory become visible. While the predicitions of KB3G and KB3G+ISB are almost indistinguishable for this part of the level scheme, there are some noticeable differences compared with the GXPF1A interaction. These differences are also reflected in the corresponding lifetime predictions, summarized in Table V. In case of the yrast 9^+ state, the KB3G interactions predict a sizable branch into the 8^+_1 state, which is hardly observed. The GXPF1A prediction is in line with latter, but has difficulties in describing the proper ratio of transitions reaching the 7^+_1 and 10^+_1 levels. None of the predicted 9^+_2 (or 9^+_3) states provides a satisfactory description of the 7352-keV 9^+_2 level, while the main decay branches of the observed 10^+_3, 10^+_4, and 10^+_5 are caught rather nicely by at least the KB3G

TABLE V. Overview of experimental [14] and predicted lifetimes of near-yrast states in ^{54}Fe.

E_x (keV)	I_i^π ($\hbar$)	$\tau_{\rm exp}$ (ps)	KB3G (ps)	+ISB (ps)	GXPF1A (ps)
1408	2^+_1	1.10(3)	1.6	1.5	1.3
2537	4^+_1	5.8(12)	6.3	5.9	7.6
2561[a]	0^+_2	$\geqslant 2$	18	14	7.1
2948	6^+_1	1760(30)	2000	1990	1900
2959[a]	2^+_2	0.075(10)	0.23	0.20	0.05
3166[a]	2^+_3	$0.22(^{6}_{4})$	0.04	0.04	0.18
3294	4^+_2	$\geqslant 3$	0.77	0.83	0.23
3344	3^+_1		14	16	11
3833[a]	4^+_3	0.089(17)	0.23	0.20	1.4
4031	5^+_1	$\geqslant 1$	1.2	1.2	0.87
4048	4^+_4	$0.43(^{33}_{14})$	0.37	0.31	0.10
4072[a]	3^+_2	0.084(25)	0.20	0.15	0.07
4656	5^+_2		0.18	0.17	0.29
5046	6^+_2		0.02	0.02	0.03
5280	6^+_3		0.09	0.09	0.27
5928	7^+_1		0.06	0.06	0.05
6300	7^+_2		0.12	0.08	0.01
6380	8^+_1	$0.16(^{4}_{3})$	0.08	0.07	0.03
6526	10^+_1	525000(10000)	514000	502000	519000
6724	9^+_1	≈ 60	11	13	21
6865	8^+_2		0.04	0.04	0.05
7076	8^+_3		0.02	0.02	0.04
7352	9^+_2		0.32	0.36	0.95
7504	10^+_2		0.18	0.17	0.24
8019	11^+_1		0.04	0.04	0.04
8808	11^+_2		0.05	0.05	0.06
9846	12^+_1		0.10	0.10	0.04
10131	12^+_2		0.04	0.04	0.03
11093	13^+_1		0.06	0.06	0.04
12314	14^+_1		0.10	0.08	0.38
12954	14^+_2		0.01	0.01	0.01
14386	15^+_1		0.01	0.01	0.02
15631	16^+_1	unmatched			
16005	16^+_2		0.02	0.02	0.03

[a]Not observed in the present experiment.

calculations. The same can be said about the 14^+_1, 15^+_1, and 15^+_2 states, with which GXPF1A has problems to describe the observed feedings and decay pattern. In the case of the 8808-keV 11^+_2 level, all parameterizations fail to predict the rather intense 2282-keV, $11^+_2 \rightarrow 10^+_1$ branch. At variance, the decay pattern of the yrast and yrare 12^+ states is very well in line with the GXPF1A predictions, while it was necessary to exchange the sequence of the two corresponding states for the KB3G calculations in order to achieve good agreement between theory and experiment for feeding and decay pattern concerning these two states. Taking a closer look into the predicted main partitions of wave functions of all these intermediate spin states, it turns out that they are very similar and highly mixed in all cases. Thus, small differences in residual interactions can lead to rather significant changes in decay pattern while the predicted energies remain essentially unaffected.

The most interesting result is that the shell-model calculations cannot provide a candidate for yrast 16^+_1 state observed at 15631 keV, which is part of the more collectively appearing part of the level scheme named Q1. In turn, the predicted yrast 16^+_1 state can be readily associated with the experimental 16005-keV 16^+_2 state, which is seemingly concluding the central, shell-model-type sequence of the level scheme.

The predicted lifetimes in this part of the level scheme are mostly short and can be hardly distinguished for the different parameterizations. Those states which do reveal rather different predictions, for example, the yrast and yrare 9^+ and the yrast 14^+ states, can be readily assessed by means of (non)matching branching ratios, as discussed earlier.

The left-hand side of Fig. 1, labeled Q1 (cf. Sec. V B 1), sees occasional matches of observed and predicted branching ratios for some medium-spin states. This allows us to associate observed and predicted states with reasonable confidence. These are, for instance, the 5482-keV 6^+_4, the 5884-keV 6^+_5 (only GXPF1A), the 6551-keV 7^+_3, the 7076-keV 8^+_3, or the 7254-keV 8^+_4 states. It turns out that this is neither feasible nor reasonable for the 9^+-15^+ nonyrast states in that section of the level scheme, thereby checking up to ten calculated states per spin value. The experimental 15631-keV 16^+_1 state is discussed above. There is an overall somewhat better agreement with the GXPF1A parameterization, which might be associated with its partially empirical nature [34].

The negative-parity "$M1$ cascades" D3 and D4 (cf. Fig. 1) are by default outside the model space of the present shell-model calculations (cf. Sec. V B).

2. *Notes on* ^{53}Mn

The shell-model predictions and comparisons with experimental observables are summarized in the lower part of Table III. Branching ratios are listed in Table VI, and lifetimes are compared in Table VII. Shell-model configurations and their maximum possible spin values are presented in Table VIII.

With $Z = 25$ and $N = 28$, the low- to medium-spin yrast structure of ^{53}Mn should and does represent a shell-model case par excellence. Starting from the 7961-keV $25/2^-_1$ state, indeed the decay pattern toward the $7/2^-$ ground state

TABLE VI. Selection of experimental (Table II and Ref. [16]) and predicted branching ratios of excited states in ^{53}Mn. Energies of unobserved (n.o.) γ-ray transitions are listed in italic characters. Spin-parity labels in square brackets, $[I^\pi_i]$, represent suggested theoretical assignments. The column labeled "set" refers to the classification of states used for MLD, BES, and MBD assessments (cf. Table III).

E_x (keV)	set[a]	E_γ (keV)	I^π_i ($\hbar$)	I^π_f ($\hbar$)	$b_{\rm exp}$	KB3G	+ISB	GXPF1A
1290[b]	yy	913	$3/2^-_1$	$5/2^-_1$	46(2)	32	32	57
		1290		$7/2^-_1$	54(2)	68	68	43
1620	y	*179*	$9/2^-_1$	$11/2^-_1$	n.o.	0	0	0
		1243		$5/2^-_1$	26(5)	18	18	14
		1620		$7/2^-_1$	74(5)	82	82	85
2274[b]	yy	*654*	$5/2^-_2$	$9/2^-_1$	n.o.	0	0	0
		984		$3/2^-_1$	4(1)	0	0	0
		1897		$5/2^-_1$	22(2)	23	25	37
		2274		$7/2^-_1$	74(2)	77	75	63
2407[b]	yy	*133*	$3/2^-_2$	$5/2^-_2$	n.o.	0	0	0
		1117		$3/2^-_1$	47(2)	12	15	22
		2030		$5/2^-_1$	13(1)	19	9	16
		2407		$7/2^-_1$	40(2)	69	76	62
2563	y	*943*	$13/2^-_1$	$9/2^-_1$	n.o.	0	0	0
		1122		$11/2^-_1$	100	100	100	100
2573[b]	yy	*299*	$7/2^-_2$	$5/2^-_2$	n.o.	3	2	1
		953		$9/2^-_1$	n.o.	3	3	2
		1132		$11/2^-_1$	n.o.	0	0	0
		1283		$3/2^-_1$	n.o.	0	0	0
		2196		$5/2^-_1$	62(1)	71	76	78
		2573		$7/2^-_1$	38(1)	23	19	18
2671[b]	yy	264	$1/2^-_1$	$3/2^-_2$	23(1)	1	9	2
		397		$5/2^-_2$	n.o.	0	0	0
		1381		$3/2^-_1$	31(1)	91	59	98
		2294		$5/2^-_1$	46(1)	8	32	0
2692	y	129	$15/2^-_1$	$13/2^-_1$	0(1)	0	0	1
		1252		$11/2^-_1$	100(1)	100	100	99
2697	yy	*124*	$11/2^-_2$	$7/2^-_2$	n.o.	0	0	0
		134		$13/2^-_1$	9(2)	15	12	5
		1077		$9/2^-_1$	43(4)	56	47	69
		1255		$11/2^-_1$	32(4)	21	29	26
		2697		$7/2^-_1$	16(3)	7	13	0
2947[b]	yy	*250*	$9/2^-_2$	$11/2^-_2$	n.o.	0	0	0
		374		$7/2^-_2$	n.o.	3	2	1
		384		$13/2^-_1$	n.o.	0	0	0
		673		$5/2^-_2$	n.o.	0	0	0
		1327		$9/2^-_1$	n.o.	11	10	2
		1506		$11/2^-_1$	3(2)	4	3	2
		2570		$5/2^-_1$	n.o.	5	7	6
		2947		$7/2^-_1$	97(2)	77	77	90
3424	yy	*477*	$13/2^-_2$	$9/2^-_2$	n.o.	0	0	0
		728		$11/2^-_2$	75(5)	69	69	37
		732		$15/2^-_1$	n.o.	11	8	22
		861		$13/2^-_1$	13(2)	3	4	18
		1804		$9/2^-_1$	n.o.	0	0	0
		1984		$11/2^-_1$	12(3)	16	19	23
3439	yy	*742*	$15/2^-_2$	$11/2^-_2$	n.o.	0	0	0
		747		$15/2^-_1$	74(1)	78	74	87
		876		$13/2^-_1$	20(1)	17	22	6
		1998		$11/2^-_1$	6(1)	5	5	6

TABLE VI. (*Continued.*)

E_x (keV)	set[a]	E_γ (keV)	I_i^π ($\hbar$)	I_f^π ($\hbar$)	$b_{\exp}$	KB3G	+ISB	GXPF1A
4310	a	*193*	$15/2^-_3$	$13/2^-_3$	n.o.	0	0	0
		871		$15/2^-_2$	10(1)	1	2	1
		885		$13/2^-_2$	9(1)	4	5	0
		1613		$11/2^-_2$	n.o.	3	3	1
		1617		$15/2^-_1$	82(3)	57	60	0
		1747		$13/2^-_1$	n.o.	34	30	84
		2869		$11/2^-_1$	n.o.	0	0	14
4383	y	*73*	$17/2^-_1$	$15/2^-_3$	n.o.	0	0	0
		266		$13/2^-_3$	n.o.	0	0	0
		944		$15/2^-_2$	63(1)	60	62	39
		959		$13/2^-_2$	n.o.	0	0	0
		1691		$15/2^-_1$	23(1)	23	21	49
		1820		$13/2^-_1$	15(1)	17	17	12
4614	a	*1175*	$15/2^-_4$	$15/2^-_2$	n.o.	5	4	19
		1921		$15/2^-_1$	22(7)	15	15	36
		2050		$13/2^-_1$	43(6)	76	75	18
		3173		$11/2^-_1$	35(6)	4	5	19
5099	yy	485	$17/2^-_2$	$15/2^-_4$	11(2)	7	7	9
		716		$17/2^-_1$	12(2)	10	9	17
		789		$15/2^-_3$	11(2)	3	3	12
		982		$13/2^-_3$	n.o.	0	0	0
		1660		$15/2^-_2$	9(1)	18	17	7
		1675		$13/2^-_2$	13(2)	11	11	18
		2407		$15/2^-_1$	43(3)	48	51	36
		2536		$13/2^-_1$	n.o.	2	2	2
5613	y	*514*	$19/2^-_1$	$17/2^-_2$	n.o.	0	0	0
		999		$15/2^-_4$	n.o.	0	0	0
		1230		$17/2^-_1$	72(1)	70	69	54
		1303		$15/2^-_3$	n.o.	0	0	0
		2174		$15/2^-_2$	27(1)	28	29	26
		2922		$15/2^-_1$	1(1)	2	2	20
5642	a	*1028*	$17/2^-_3$	$15/2^-_4$	n.o.	8	8	1
		1259		$17/2^-_1$	n.o.	4	3	4
		2203		$15/2^-_2$	57(7)	19	21	50
		2950		$15/2^-_1$	43(7)	67	66	41
5771	a	3208	[$17/2^-_4$]	$13/2^-_1$	100	60	59	15
5928						unmatched		
6092						unmatched		
6264	yy	622	$19/2^-_2$	$17/2^-_3$	11(2)	21	18	4
		651		$19/2^-_1$	n.o.	0	0	1
		1165		$17/2^-_2$	n.o.	3	3	4
		1241		$15/2^-_5$	n.o.	0	0	1
		1650		$15/2^-_4$	n.o.	1	1	0
		1881		$17/2^-_1$	60(4)	56	58	58
		1954		$15/2^-_3$	7(1)	16	15	13
		2825		$15/2^-_4$	n.o.	2	3	0
		3572		$15/2^-_1$	21(3)	1	1	19
6297	a	1914	$19/2^-_3$	$17/2^-_1$	100	43	45	21
		2858		$15/2^-_2$	n.o.	21	22	37
		3605		$15/2^-_1$	n.o.	19	16	18
6458	a	816	$19/2^-_4$	$17/2^-_3$	14(3)	8	5	0
		845		$19/2^-_1$	n.o.	14	13	3
		1359		$17/2^-_2$	n.o.	40	28	21
		1844		$15/2^-_4$	n.o.	21	22	8
		2075		$17/2^-_1$	75(5)	7	4	13
		2148		$15/2^-_3$	12(3)	3	1	0

TABLE VI. (*Continued.*)

E_x (keV)	set[a]	E_γ (keV)	I_i^π ($\hbar$)	I_f^π ($\hbar$)	$b_{\exp}$	KB3G	+ISB	GXPF1A
		3766		$15/2^-_1$	n.o.	3	26	47
6533	y	*75*	$21/2^-_1$	$19/2^-_4$	n.o.	0	0	0
		236		$19/2^-_3$	0(1)	0	0	0
		269		$19/2^-_2$	1(1)	1	1	1
		762		$17/2^-_4$	n.o.	0	0	0
		891		$17/2^-_3$	n.o.	0	0	0
		920		$19/2^-_1$	28(1)	27	30	27
		1434		$17/2^-_2$	n.o.	0	0	0
		2150		$17/2^-_1$	70(1)	72	69	72
6654		3963	17/2	$15/2^-_1$		unmatched		
6683	a	1584	$19/2^-_5$	$17/2^-_2$	30(8)	1	1	6
		2300		$17/2^-_1$	n.o.	24	20	15
		3244		$15/2^-_2$	18(6)	1	4	5
		3991		$15/2^-_1$	52(10)	70	58	70
6822		4128	[$19/2^-_6$]	$15/2^-_1$	100	84	62	62
7004	y	*321*	$23/2^-_1$	$19/2^-_5$	n.o.	0	0	0
		471		$21/2^-_1$	84(1)	84	86	83
		546		$19/2^-_4$	n.o.	0	0	0
		707		$19/2^-_3$	n.o.	0	0	0
		740		$19/2^-_2$	0(1)	1	1	2
		1391		$19/2^-_1$	15(1)	16	13	15
7017	yy	334	$21/2^-_2$	$19/2^-_5$	5(1)	0	0	0
		484		$21/2^-_1$	18(2)	11	11	10
		559		$19/2^-_4$	2(1)	37	37	16
		1918		$17/2^-_2$	75(3)	48	47	63
7224			19/2			Unmatched		
7315	a	*1051*	$21/2^-_3$	$19/2^-_2$	n.o.	16	17	2
		1702		$19/2^-_1$	100	62	63	32
		2932		$17/2^-_1$	n.o.	0	0	41
7360						Unmatched		
7406	a	*1109*	$21/2^-_4$	$19/2^-_3$	n.o.	16	17	2
		1141		$19/2^-_2$	40(4)	1	1	31
		1793		$19/2^-_1$	n.o.	6	5	45
		3023		$17/2^-_1$	60(4)	53	48	1
7600	a	*596*	$21/2^-_5$	$23/2^-_1$	n.o.	21	15	7
		1142		$19/2^-_4$	n.o.	0	0	17
		1303		$19/2^-_3$	n.o.	13	13	8
		1336		$19/2^-_2$	30(6)	37	32	25
		1958		$17/2^-_3$	15(6)	4	5	1
		1987		$19/2^-_1$	55(8)	8	13	24
7961	y	*361*	$25/2^-_1$	$21/2^-_5$	n.o.	0	0	0
		555		$21/2^-_4$	n.o.	0	0	0
		646		$21/2^-_3$	n.o.	0	0	0
		944		$21/2^-_2$	n.o.	0	0	0
		957		$23/2^-_1$	92(1)	93	93	94
		1428		$21/2^-_1$	8(1)	7	7	6
7979	yy	*573*	$23/2^-_2$	$21/2^-_4$	n.o.	2	0	8
		664		$21/2^-_3$	n.o.	24	20	0
		962		$21/2^-_2$	32(2)	28	34	26
		975		$23/2^-_1$	n.o.	3	3	2
		1446		$21/2^-_1$	n.o.	8	8	13
		1521		$19/2^-_4$	n.o.	1	1	0
		1715		$19/2^-_2$	n.o.	5	3	3
		2366		$19/2^-_1$	68(2)	29	31	47
8022			21/2			Unmatched		

TABLE VI. (*Continued.*)

E_x (keV)	set[a]	E_γ (keV)	I_i^π ($\hbar$)	I_f^π ($\hbar$)	$b_{\rm exp}$	KB3G	+ISB	GXPF1A
8237		832	$(23/2^-_3)$	$21/2^-_4$	16(3)	17	12	4
		1220		$21/2^-_2$	72(5)	3	3	1
		1233		$23/2^-_1$	n.o.	10	13	20
		1780		$19/2^-_4$	13(3)	7	7	0
		1940		$19/2^-_3$	n.o.	0	0	24
		1973		$19/2^-_2$	n.o.	37	39	0
		2624		$19/2^-_1$	n.o.	10	10	29
8452		1046	$(23/2^-_4)$	$21/2^-_4$	25(5)	16	17	7
		1136		$19/2^-_4$	52(9)	1	1	27
		1448		$23/2^-_1$	n.o.	21	20	1
		1919		$21/2^-_1$	n.o.	11	12	34
		2155		$19/2^-_3$	n.o.	20	17	1
		2188		$19/2^-_2$	23(7)	6	8	16
		2839		$19/2^-_1$	n.o.	22	25	10
8744			23/2			Unmatched		
9032			23/2			Unmatched		
9402	yy	*1165*	$25/2^-_2$	$23/2^-_3$	n.o.	5	5	3
		1423		$23/2^-_2$	29(4)	33	34	9
		1441		$25/2^-_1$	n.o.	27	27	33
		1802		$21/2^-_5$	n.o.	0	0	3
		1997		$21/2^-_4$	9(2)	1	1	1
		2086		$21/2^-_3$	10(2)	0	1	17
		2385		$21/2^-_2$	n.o.	15	13	2
		2397		$23/2^-_1$	27(4)	13	14	6
		2869		$21/2^-_1$	25(3)	5	6	26
9580	a	1343	$25/2^-_3$	$23/2^-_3$	27(5)	32	32	14
		1601		$23/2^-_2$	n.o.	1	1	20
		1620		$25/2^-_1$	30(4)	27	26	23
		2174		$21/2^-_4$	n.o.	17	17	1
		2563		$21/2^-_2$	14(3)	6	8	29
		2576		$23/2^-_1$	29(5)	0	0	13
		3047		$21/2^-_1$	n.o.	14	13	0
10106			25/2			Unmatched		
10381	yy	801	$27/2^-_1$	$25/2^-_3$	20(4)	1	1	6
		979		$25/2^-_2$	n.o.	19	19	0
		1929		$23/2^-_4$	n.o.	2	3	7
		2144		$23/2^-_3$	1(1)	16	15	0
		2402		$23/2^-_2$	n.o.	23	21	20
		2420		$25/2^-_1$	78(5)	24	26	65
		3377		$23/2^-_1$	n.o.	15	15	2
10413		1669		23/2		Unmatched		
10708	yy	*1128*	$27/2^-_2$	$25/2^-_3$	n.o.	3	3	1
		1307		$25/2^-_2$	9(2)	6	6	1
		2256		$23/2^-_4$	n.o.	18	15	1
		2471		$23/2^-_3$	n.o.	3	3	29
		2730		$23/2^-_2$	23(4)	3	3	3
		2747		$25/2^-_1$	23(4)	10	13	14
		3705		$23/2^-_1$	45(7)	57	56	51
11017	a	*2565*	$27/2^-_3$	$23/2^-_4$	n.o.	16	20	3
		2780		$23/2^-_3$	n.o.	2	4	19
		3056		$25/2^-_1$	16(4)	17	12	34
		4014		$23/2^-_1$	84(4)	52	52	35
11264			27/2			Unmatched		
11525		*1945*	$[27/2^-_4]$	$25/2^-_3$	n.o.	30	30	1
		2123		$25/2^-_2$	n.o.	2	3	21
		3564		$25/2^-_1$	100	57	58	66

TABLE VI. (*Continued.*)

E_x (keV)	set[a]	E_γ (keV)	I_i^π ($\hbar$)	I_f^π ($\hbar$)	$b_{\rm exp}$	KB3G	+ISB	GXPF1A
11705		1292	$27/2^-_5$	$25/2^-_4$	23(9)	2	1	1
		3744		$25/2^-_1$	77(9)	73	71	94
11823	yy	806	$29/2^-_1$	$27/2^-_3$	7(3)	10	9	4
		1115		$27/2^-_2$	n.o.	1	1	1
		1410		$25/2^-_4$	n.o.	0	0	0
		1442		$27/2^-_1$	n.o.	6	6	3
		2243		$25/2^-_3$	25(5)	59	63	7
		2421		$25/2^-_2$	58(7)	1	1	32
		3863		$25/2^-_1$	10(3)	24	20	54
12068		4107	$[27/2^-_6]$	$25/2^-_1$	100	43	38	16
12216			29/2			Unmatched		
12467	yy	1449	$29/2^-_2$	$27/2^-_3$	14(4)	12	16	16
		4505		$25/2^-_1$	86(4)	75	70	72
12817		749	$[29/2^-_4]$	$27/2^-_6$	46(23)	0	1	0
		4856		$25/2^-_1$	54(23)	69	69	45
13081		2372	$[31/2^-_1]$	$27/2^-_2$	100	61	61	52
13176			31/2			Unmatched		
13809		1343	$[31/2^-_2]$	$29/2^-_2$	100	47	49	54
14092		1625	$[31/2^-_3]$	$29/2^-_2$	100	38	32	22

[a]y: yrast structure; yy: plus yrare states; a: all mapped states.
[b]Not observed in the present experiment.

is extraordinarily well described by the KB3G interaction and extremely well by the GXPF1A interaction, the former including essentially all minor observed side branches into nonyrast levels as well. Notably, once including the isospin-

TABLE VII. Overview of experimental [16] and predicted lifetimes of near-yrast states in ^{53}Mn.

E_x (keV)	I_i^π ($\hbar$)	$\tau_{\rm exp}$ (ps)	KB3G (ps)	+ISB (ps)	GXPF1A (ps)
378	$5/2^-_1$	169(9)	187	209	59
1290[a]	$3/2^-_1$	$0.79(^{6}_{5})$	2.0	1.9	1.1
1441	$11/2^-_1$	0.87(12)	1.4	1.4	1.3
1620	$9/2^-_1$	0.69(9)	1.3	1.2	1.1
2274[a]	$5/2^-_2$	0.36(7)	0.78	0.71	0.65
2563	$13/2^-_1$	15.5(18)	21.5	24.1	14.7
2573[a]	$7/2^-_2$	0.09(3)	0.19	0.15	0.09
2692	$15/2^-_1$	3.9(6)	5.9	5.8	8.1
3424	$13/2^-_2$	$1.0(^{6}_{4})$	2.2	2.3	2.1
3439	$15/2^-_2$	0.20(3)	0.11	0.12	0.06
4383	$17/2^-_1$	$0.23(^{8}_{7})$	0.27	0.26	0.17
5099	$17/2^-_2$		0.15	0.14	0.19
5613	$19/2^-_1$	0.17(8)	0.08	0.08	0.08
6264	$19/2^-_2$		0.07	0.11	0.07
6533	$21/2^-_1$	0.14(7)[b]	0.17	0.16	0.16
7004	$23/2^-_1$	$1.49(^{18}_{16})$[b]	1.3	1.3	2.7
7017	$21/2^-_2$		0.19	0.19	0.19
7961	$25/2^-_1$	$0.25(^{8}_{6})$	0.19	0.19	0.17
7979	$23/2^-_2$		0.10	0.10	0.12
9402	$25/2^-_2$		0.04	0.04	0.05

[a]Not observed in the present experiment.
[b]Weighted mean from Refs. [15,38].

TABLE VIII. Shell-model configurations and cranked Nilsson-Strutinsky (CNS) labels for particle-hole excitations relevant for the interpretation of the observed high-spin level schemes of ^{54}Fe and ^{53}Mn. The $p_{3/2}$ and $f_{5/2}$ shells are denoted (fp), while occupation of the $p_{1/2}$ shell is usually found to be negligible in the context of high-spin states in the mass $A \approx 50$–60 region. The CNS nomenclature is $[p_1p_2(p_3);n_1n_2(n_3)]$ with p_1 (n_1) being the number of proton (neutron) holes in orbitals of $f_{7/2}$ character, p_2 (n_2) marking the number of protons (neutrons) in orbitals of fp character, and p_3 (n_3) the number of protons (neutrons) with their dominant amplitudes in the $g_{9/2}$ shell. The numbers p_3 and n_3 are written in parentheses but omitted when they are equal to zero.

Particle-hole excitation	Shell-model configuration Protons	Neutrons	CNS label (see text)	$I_{\max}$ ($\hbar$)
^{54}Fe				
0p-2h	$f_{7/2}^{-2}$		[20; 00]	6^+
1p-3h	$f_{7/2}^{-3}(fp)$		[31; 00]	10^+
	$f_{7/2}^{-2}$	$f_{7/2}^{-1}(fp)$	[20; 11]	12^+
	$f_{7/2}^{-2}$	$f_{7/2}^{-1}g_{9/2}$	[20; 10(1)]	14^-
2p-4h	$f_{7/2}^{-2}$	$f_{7/2}^{-2}(fp)^2$	[20; 22]	16^+
	$f_{7/2}^{-2}$	$f_{7/2}^{-2}(fp)g_{9/2}$	[20; 21(1)]	19^-
	$f_{7/2}^{-2}$	$f_{7/2}^{-2}g_{9/2}^2$	[20; 20(2)]	20^+
	$f_{7/2}^{-3}(fp)$	$f_{7/2}^{-1}(fp)$	[31; 11]	16^+
	$f_{7/2}^{-3}(fp)$	$f_{7/2}^{-1}g_{9/2}$	[31; 10(1)]	18^-
	$f_{7/2}^{-3}g_{9/2}$	$f_{7/2}^{-1}(fp)$	[30(1); 11]	18^-
3p-5h	$f_{7/2}^{-3}(fp)$	$f_{7/2}^{-2}(fp)^2$	[31; 22]	20^+
^{53}Mn				
0p-3h	$f_{7/2}^{-3}$		[30; 00]	$15/2^-$
1p-4h	$f_{7/2}^{-4}(fp)$		[41; 00]	$21/2^-$
	$f_{7/2}^{-3}$	$f_{7/2}^{-1}(fp)$	[30; 11]	$27/2^-$
	$f_{7/2}^{-3}$	$f_{7/2}^{-1}g_{9/2}$	[30; 10(1)]	$31/2^+$
2p-5h	$f_{7/2}^{-3}$	$f_{7/2}^{-2}(fp)^2$	[30; 22]	$35/2^-$
	$f_{7/2}^{-4}(fp)$	$f_{7/2}^{-1}(fp)$	[41; 11]	$33/2^-$

breaking terms in the KB3G description, the predicted levels energies are also very close to the experimental values. The corresponding predicted lifetimes match the measured ones better than within a factor of 2. In turn, such a level of consistency proves that nuclei located in the $f_{7/2}$ quadrant are viable testing ground for detailed spectroscopic shell-model investigations.

Tables VI and VII provide also entries for the lowest-lying low-spin states observed in other experiments [16]. The branching ratio predictions are in general in agreement with the observed values. An interesting exception though is the 2671-keV $1/2^-$ state: Here, neither KB3G nor GXPF1A catches the decay pattern, while the inclusion of the isospin-breaking terms solves that problem. One other significant deviation is the GXPF1A lifetime prediction for the known 378-keV $5/2^-$ state, which is a factor of 3 too short. In contrast, the GXPF1A lifetime prediction for the $13/2^-_1$ state is spot on.

Moving toward the nonyrast medium-spin states between some 3- and 5-MeV excitation energy, the 2697-keV $11/2^-_2$ level is the second case for which the inclusion of ISB effects provides a noticable improvement of the decay pattern. For the other states in this category, $9/2^-_2$, $13/2^-_2$, $15/2^-_3$, and $15/2^-_4$, the decay patterns are by and large in line with the predictions with one exception, which is that the GXPF1A parameterization fails to properly describe the latter two levels, even if one were to exchange them. These are, however, worst also for KB3G.

This trend, namely that the yrare I^-_2 states are still very well described by theory, but the I^-_3 and I^-_4 to lesser and lesser extents, holds for the medium-high to high-spin regime, $I = 17/2$–$31/2$. An exception are the $19/2^-$ states, and in particular the state at 6092 keV with a tentative $19/2^-_2$ assignment in Table II. The assignment is based on the DCO ratio of the depopulating 3402-keV transition, which feeds the yrast 2692-keV, $15/2^-_1$ level. Interestingly, none of the interactions predicts a dominating $19/2^- \rightarrow 15/2^-$ branch for any of the calculated $19/2^-$ states. Thus, the experimental level found at 6092 keV remains unmatched. A possible explanation is that the 3402-keV transition is either an $M2$, $\Delta I = 2$ or mixed $M2/E1$, $\Delta I = 1$ transition. In turn, the next experimentally observed $19/2^-$ states at 6264 and 6297 keV can very well be associated with the calculated $19/2^-_2$ and $19/2^-_3$ states, respectively.

The structure labeled Q1 in the experimental level scheme in Fig. 2 cannot be identified within the lowest 10 calculated states for a given spin value. This points to significant wave-function partitions lying outside the considered shell-model space.

B. Cranked Nilsson-Strutinsky calculations

The cranked Nilsson-Strutinsky (CNS) calculations are based on the modified oscillator potential, which is cranked around a principal axis [39–41]. Here, we use the standard parameters [39] but we will also comment on results obtained with revised Nilsson parameters derived for the $A = 60$ region in Ref. [11]. Active j shells are the same as for the shell-model calculations in the preceding section, plus $1g_{9/2}$ in the $\mathcal{N} = 4$ oscillator shell. CNS configurations are classified by the number of holes in the $1f_{7/2}$ orbital and particles in either the upper fp or $1g_{9/2}$ orbitals. Note, however, that in CNS, we do not refer to the pure j shells but rather to the orbitals in the deformed rotating potential which have their dominant amplitudes in these j shells. The CNS notation $[p_1p_2(p_3);n_1n_2(n_3)]$ is used where p_1 (n_1) represents the number of proton (neutron) holes in orbitals of $f_{7/2}$ character, p_2 (n_2) represents the number of protons (neutrons) of fp character, and p_3 (n_3) represents the number of $g_{9/2}$ protons (neutrons). Labels in parentheses are omitted when equal to zero. For an odd number of particles, signature might be specified as index $+$ or $-$. An overview and comparison of relevant CNS labels with the respective shell-model configurations is given in Table VIII. The maximum possible spin, $I_{\max}$, for a given configuration is provided as well.

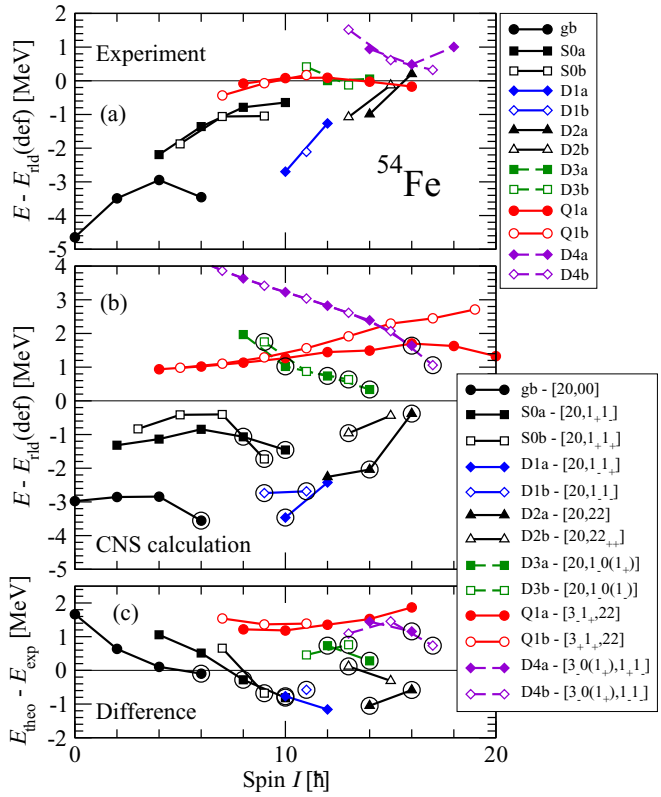

FIG. 11. Energies relative to the rotating liquid drop energy of the observed bands in ^{54}Fe [panel (a)] compared with the assigned calculated CNS configurations [panel (b)], which are detailed in Table VIII. The label "gb" represents the $(1f_{7/2}^{-2})_{0,2,4,6}$ ground band. "S0" is the dipole sequence between the 3294-keV 4^+ and 8578-keV 10^+ states. The "a" (open symbols) and "b" (filled symbols) indicate even spin (signature $\alpha = 0$) and odd spin (signature $\alpha = 1$) states, respectively. The difference between experiment and theoretical interpretation is shown in panel (c). Note that in this panel, the differences for the 10^+ states of the S0a and D1a bands overlap.

1. Notes on ^{54}Fe

^{54}Fe is situated relatively close to doubly-magic ^{56}Ni, and hence the low-spin states are close to spherical. Higher spin states are formed from excitations across the $Z = 28$ or $N = 28$ gaps which show different properties depending on whether particle excitations or hole excitations are dominating. Particle excitations prefer deformations in the upper half of the (ε_2, γ) plane with $\gamma > -30°$, while hole excitations rather lead to deformations in the lower half.

A selection of observed structures are compared with the CNS configurations assigned to them in Fig. 11. The ground band (gb) in ^{54}Fe is naturally understood as the $\pi(f_{7/2})^{-2}$ $6^+ \rightarrow 4^+ \rightarrow 2^+ \rightarrow 0^+$ cascade, i.e., the [20; 00] CNS configuration with a maximal spin of $I = 6$. The difference between experiment and theory is satisfactory and as expected for low-spin, nonrotational sequences.

The most favored excitation to create higher spin values is to lift a neutron from the $f_{7/2}$ orbitals to the fp orbitals. This leads to several CNS configurations of the type $\pi(f_{7/2})^{-2}\nu(f_{7/2})^{-1}(fp)^1$ or [20;11] in CNS notation. With signature of $\alpha = 1/2$ for the $f_{7/2}$ neutrons, this configuration nicely corresponds to the observed dipole sequence "S0" between the 3294-keV 4^+ and 8578-keV 10^+ states, as illustrated in Fig. 11. Initially, this kind of configurations has deformations $\gamma \approx 0°$, since the $f_{7/2}$ holes are not (fully) aligned. They move toward noncollective states at small prolate deformation ($\gamma = -120°$) for spin values $I = 8$–10.

The yrast 8^+-12^+ structure, D1, including the 10^+ isomer, can also be associated with [20; 11] configurations, in this case with signature $\alpha = -1/2$ for the $f_{7/2}$ neutrons. This implies that the neutron hole can be placed in the $m_i = -7/2$ orbital, contributing with the maximum spin for one hole in the $f_{7/2}$ shell. Consequently, all three $f_{7/2}$ holes are easily aligned along the prolate symmetry axis ($\gamma = -120°$), where they can contribute with $i = 3.5\hbar + 2.5\hbar + 3.5\hbar = 9.5\hbar$. One could then expect that the fp neutron would also contribute with its maximum spin, $2.5\hbar$, leading to a favored $I = 12$ state. However, on the prolate side, the $m_i = \Omega = 5/2$ orbital comes high in energy as easily seen in a Nilsson diagram. The [321]1/2 Nilsson orbital is clearly the lowest orbital at prolate shape; i.e., with the neutron in this $m_i = \Omega = 1/2$ orbital, a low-energy $I = 10$ state is formed. Indeed, this $I = 10$ state is so favored that, in agreement with experiment, it is calculated at an energy similar to that of the $I = 8$ state of this [20; 11] configuration. Furthermore, also the $I = 11$ and $I = 12$ states of this configuration are in good agreement with experiment; see Fig. 11.

To obtain positive-parity states with $I > 12$, another neutron can be excited to the fp orbitals, which leads to [20; 22] CNS configurations with $I_{max} = 16$. This provides the best explanation for the observed yrast D2, $I = 13$–16 states. Note that the odd-spin states must be formed with two particles (or holes) having the same signature; in this case the two fp particles have $\alpha = +1/2$. The deformation for these $I = 13$–16 states is also in the third sector; i.e., the $f_{7/2}$ holes are close to fully aligned at low frequencies, suggesting a band-head spin around $2(3.5\hbar + 2.5\hbar) = 12\hbar$ and consistent with the fact that only high-spin states have been observed in this sequence. We have also tested configurations with one proton and one neutron excited across the $N, Z = 28$ gap, but these configurations are calculated considerably higher in energy than those with two neutrons excited across the $N = 28$ gap.

The next band in the yrast region which we will consider is D3 (cf. Fig. 1), which has negative parity. Therefore, it has either one particle excited to $g_{9/2}$ or a hole in the $\mathcal{N} = 2$ orbitals. The energy costs for these excitations are similar but higher spins are formed with $g_{9/2}$ particles. Thus, we expect to observe configurations with one $g_{9/2}$ particle. The corresponding predicted lowest-energy states have one neutron excited across the $N = 28$ gap and that neutron is placed into the lowest orbital of $g_{9/2}$ character: [20; 10(1)] in CNS nomenclature. This configuration is dominated by holes which means that deformation will mainly be in the third sector. Therefore, it is the two possible signatures of the $g_{9/2}$ neutron which leads to signature degenerate bands, not the $f_{7/2}$ holes. The three $f_{7/2}$ holes will create a band head with $I \approx 3.5\hbar + 2.5\hbar + 3.5\hbar = 9.5\hbar$, i.e., $I = 9$ or 10. This is the lowest negative-parity configuration which is naturally

assigned to the observed band D3 (cf. Fig. 1). As seen in Fig. 11, these bands are calculated somewhat too high in energy. With the revised parameters of Ref. [11], the $g_{9/2}$ shell is placed at a lower energy, leading to a better agreement with experiment. Note that the maximum terminating spin $I = 14$ is experimentally reached for this configuration assignment.

The band D4 shows a pronounced signature degeneracy, indicating that the observed 18^- state at 19589 keV does not belong to the same band. The signature degeneracy of D4 suggests that it is based on unpaired $f_{7/2}$ holes, because configurations with one hole in a high-j shell are known to generate signature degeneracy at $\gamma > -30^\circ$. Thus, to obtain negative parity and spins up to $I = 17$, choices are the 2p-4h $[30(1); 11]$ or $[31; 10(1)]$ CNS configurations, which both provide $I_{\max} = 18$. With standard parameters, the $[30(1); 11]$ configuration is favored, where the signature combination shown in Fig. 11 is calculated to be lowest in energy. These configurations see a proton in the $g_{9/2}$ orbital. Though rather constant as function of spin if the 18^- state is excluded, the difference between calculations and experiment is somewhat too large, but it falls into the same range as the differences for other structures, as can be seen in the bottom panel of Fig. 11. Configuration mixing between bands $[30(1); 11]$ and $[31; 10(1)]$, i.e., with either a proton or a neutron in $g_{9/2}$, can lower the predicted energies but otherwise keep the signature degeneracy. Interestingly, a CNS calculation with the revised $A = 60$ parameters [11] favors the neutron $g_{9/2}$ excitation. The 2p-4h assignment to D4 is also consistent with the observation of rather intense $E2$ decays from D4 into D3, which is interpreted as a 1p-3h band: $E2$ (re)coupling across $N, Z = 28$ is strong for the involved $f_{7/2}$ and $p_{3/2}$ orbitals.

The negative-parity configuration reaching somewhat higher spins, $I_{\max} = 19$, and calculated at similar excitation energies, is $[20; 21(1)]$. However, it can be excluded as explanation for D4 because it does not explain the signature degeneracy and it does not form any regular bands in the calculations. Possibly, the 18^- state at 19589 keV, which is drawn as a member of band D4 in Fig. 11, the two levels on top, and the yrare 17^- state at 18068 keV belong to that structure. Furthermore, though 3p-5h $[30(1); 22]$ configurations are also found competitive in energy, they cannot explain the signature degeneracy either.

The last band to consider is Q1, which is observed up to $I = 16$ (cf. Fig. 1). Because of the positive parity, all the valence particles are in the $\mathcal{N} = 3$ shell or, alternatively, two are excited to the $\mathcal{N} = 4$ shell rather than from the $\mathcal{N} = 2$ shell due to the need for high spin. However, in the CNS calculations, these excitations cost too much energy; i.e., for Q1 the CNS model predicts that in leading order all valence particles are in the $\mathcal{N} = 3$ shell. The highest observed spin in the Q1 band, $I = 16$, can in principle be reached with two particles excited across the 28 gap, namely in 2p-4h configurations of the type $[20; 22]$ or $[31; 11]$. However, only the $I = 16$ state of the former configuration better fits to the 16005-keV level, which in conjunction with the 15^+, 14^+, and 13^+ states below forms, in the CNS language, a dipole band, D2. More importantly, none of these configurations forms any collective structures of the type observed for the Q1 band. Thus, 3p-5h-type CNS configurations $[31; 22]$ with $I_{\max} = 20$ are assigned to Q1. Toward high spin, the favored signatures are those which create the $I_{\max} = 20$ state, as shown in Fig. 11. The assignment is in nice agreement with the observed signature partner Q1b at medium-spin values, $I = 7, 9, 11$: At these spin values, the two signature partners ($f_{7/2}$ proton hole or fp proton) have very similar energies such that Q1a can be assigned to one or the other. At these intermediate spin, deformation parameters $\varepsilon_2 \sim 0.25$ at $\gamma \sim 0^\circ$ are predicted. Variations of occupations of proton and neutron, $p_{3/2}$ and $f_{5/2}$ orbitals can readily explain the related side bands of Q1 in the intermediate spin range.

For the assignment of the Q1 bands, we have followed the collective minima of the $[31; 22]$ configurations, neglecting a few less collective states with $\gamma \approx -120^\circ$ at lower energy. The comparison between experiment and calculations for the Q1 bands in Fig. 11 gives a difference which is rather constant as function of spin, but too high in energy, approaching $+2$ MeV. Interestingly, this number is similar to an estimate based on Fig. 3 of Ref. [3] (cf. VAP 4p-4h). The authors assess the possibility of collective states in the $N = 28$ isotone series with more advanced shell-model techniques.

Similar to the note at the end of the paragraph on D4, configuration mixing with other positive-parity bands calculated nearby can lead to a downshift in energy of the lowest (observed) band. Possible candidates are 2p-4h $[20; 20(2)]$ and $[30(1); 10(1)]$ configurations, involving two particles in the $g_{9/2}$ orbital. Recalling the shell-model result concerning Q1 (see Sec. V A), a consistent picture evolves: Given that in particular the higher lying members of the experimental band *cannot* be identified among the first ten calculated shell-model states points toward significant contributions of partitions *outside* the full fp model space, namely excitations of nucleon pairs into the $g_{9/2}$ orbital, which is known to give rise to well-deformed rotational bands in and beyond ^{56}Ni [2,11].

2. *Notes on* ^{53}Mn

A selection of observed structures in the semimagic $N = 28$ isotone ^{53}Mn are compared with the assigned CNS configurations in Fig. 12. The ground band (gb) is formed with a closed $N = 28$ core and three $f_{7/2}$ proton holes, leading to a maximum spin of $15/2^-$ for this $[30; 00]$ configuration. These calculated bands in the low-spin yrast region start from small prolate deformation, $\varepsilon_2 \approx 0.1$, and terminate close to spherical shape.

Higher spin states are formed with at first neutrons excited across the $N = 28$ gap, leading to nonsmooth energies and several noncollective states, i.e., $[30; 11]$ CNS configurations with various possibilities to place particles in orbitals of different signature. The yrast sequence between the 3439-keV $15/2^-$ and 7961-keV $25/2^-$ states, denoted S0 in Fig. 12, is best described by $[3\_0; 1\_1\_]$ and $[3\_0; 1\_1_+]$ signature partners. The shape of the signature $\alpha = +1/2$ ($[3\_0; 1\_1\_]$) cascade evolves rather smoothly from small prolate deformations, $\varepsilon_2 \approx 0.15$, to noncollective prolate, $\gamma = -120^\circ$, at termination. The $23/2^-$ and $27/2^-$ states of the signature partner can be compared with the 10^+ isomer and related 12^+ state in ^{54}Fe, but with an additional $m_i = -3/2$ $f_{7/2}$ neutron hole. These states in ^{53}Mn are thus built with the spin

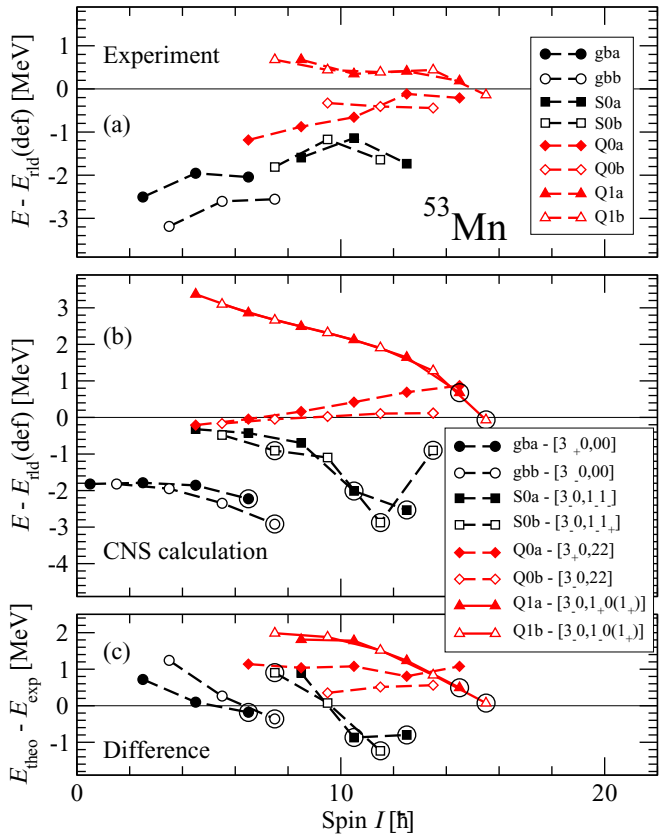

FIG. 12. Energies relative to the rotating liquid drop energy of the observed bands in ^{53}Mn [panel (a)] compared with the assigned calculated CNS configurations [panel (b)], which are detailed in Table VIII. The label "gb" represents the $(f_{7/2}^{-3})$ ground band up to spin $15/2^-$. "S0" is the yrast sequence between the 3439-keV 15^-_2 and 7961-keV $25/2^-$ states. The "a" (open symbols) and "b" (filled symbols) indicate signature $\alpha = +1/2$ and signature $\alpha = -1/2$ states, respectively. The CNS energies in panel (b) for the [30; 22] configuration are extracted from the collective close-to-prolate minimum. The difference between experiment and theoretical interpretation is shown in panel (c).

vector aligned along the prolate symmetry axis where the four $f_{7/2}$ neutron holes contribute with a spin of $7/2\hbar + 5/2\hbar + 3/2\hbar + 7/2\hbar = 11\hbar$ with the proton in either the lowest $m_i = \Omega = 1/2$ or the $m_i = \Omega = 5/2$ fp Nilsson orbital. The $27/2^-$ state is thus calculated at a relatively high energy and might be assigned to the observed 10708-keV state.

With two neutrons excited, the configuration calculated lowest in energy is [30; 22]. In this configuration, a collective prolate minimum ($\varepsilon_2 \approx 0.2$) can be followed for intermediate spins. However, noncollective states at lower energy are calculated in several cases, especially at high spin. As seen in Fig. 12, the bands in the collective minimum give a reasonable description for the cascades drawn in the central part of the level scheme of ^{53}Mn in Fig. 2, for instance, the 2243-2563-1918-1675-keV Q0 sequence, which is also described in connection with the experimental spectrum in Fig. 8.

An alternative to the excitation of a second neutron across the $N = 28$ to reach higher spin values is to place it into the $g_{9/2}$ orbital rather than the upper fp shell. This gives rise to [30; 10(1)] configurations, which are predicted to be signature degenerate and to have a rather stable deformation of $\varepsilon_2 \approx 0.2$ and $\gamma \approx 10^\circ$ prior to favored termination near sphericity at their $I_{max} = 29/2$ and $31/2$, respectively. The observed band Q1 band is regular with the highest spin states favored in energy. This suggests that the band is approaching termination or that it has even reached the terminating state. Indeed, this feature is very well described if the signature partners of the band are assigned to the [3_0; 1_0(1_+)] and [3_0; 1_+0(1_+)] configurations as done in Fig. 12. With this assignment, Q1 has positive parity and has reached the $I_{max} = 31/2$ terminating state. One may add that compared with the excitation to the fp orbitals, [30; 11], the general shape of the $E - E_{rld}$ curve and the deformation trajectories show similarities, but the deformation is larger and the $E - E_{rld}$ curve is more regular in the case when the neutron is excited to the $g_{9/2}$ orbital. Finally, the [30; 10(1)] assignment to Q1 in ^{53}Mn is also in line with the earlier observation and [30; 30(1)] interpretation of a similar rotational structure in ^{51}Mn, where termination takes place at $I_{max} = 39/2$, due to the additional two neutron holes in $f_{7/2}$ orbitals [12].

VI. SUMMARY AND CONCLUSIONS

Largely extended high-spin level schemes of the $N = 28$ semimagic isotones ^{54}Fe and ^{53}Mn are presented. A thorough and detailed comparison of excitation energies and electromagnetic decay properties with large-scale shell-model calculations in the fp shell is described. Yrast and yrare states are typically very well understood, both in terms of excitation energies and decay patterns. With increasing distance to the yrast line, these predictions become less conclusive. In particular, for high-spin states in ^{54}Fe, the aforementioned difficulties can be associated with an increasing influence of particle-hole excitations across the $Z = 28$ and $N = 28$ gaps, which are essential in doubly magic ^{56}Ni [2].

For the states amenable to a shell-model description, it is found that in general KB3G performs somewhat better than GXPF1A and that the KB3G predictions improve by including isospin-breaking terms.

Cranked Nilsson-Strutinsky calculations can deal with a larger configuration space and allow us to describe the collective structures observed in both $N = 28$ isotones. For the negative-parity dipole structures seen in ^{54}Fe, the simplest description involves the excitation of one neutron into the $g_{9/2}$ intruder orbital. Mixing with configurations involving a corresponding proton excitation is likely. Similarly, contributions from pair excitations into the $g_{9/2}$ orbital can lower the predicted quadrupole bands and, at the same time, admixtures of such type of excitations provide an explanation for shell-model deficiencies at high spins. Furthermore, the CNS calculations provide an illustrative description of the 10^+ isomer in ^{54}Fe, as built from three $f_{7/2}$ holes with their spin vectors aligned along the prolate symmetry axis contributing with $9.5\hbar$, while the additional $0.5\hbar$ is given by a neutron in the lowest fp Nilsson orbital.

ACKNOWLEDGMENTS

We would like to thank the accelerator crews and the Gammasphere support staff at Argonne and Berkeley for their supreme efforts. This research used resources of ANL's ATLAS facility, which is a DOE Office of Science User Facility. This work is supported in part by the Swedish Research Council (Vetenskapsrådet, VR 2016-3969) and the U.S. Department of Energy under Grants No. DE-AC02-05CH11231 (LBNL), No. DE-AC02-06CH11357 (ANL), and No. DE-FG05-88ER-40406 (WU).

[1] E. Ideguchi, D. G. Sarantites, W. Reviol, A. V. Afanasjev, M. Devlin, C. Baktash, R. V. F. Janssens, D. Rudolph, A. Axelsson, M. P. Carpenter *et al.*, Phys. Rev. Lett. **87**, 222501 (2001).

[2] D. Rudolph, C. Baktash, M. J. Brinkman, E. Caurier, D. J. Dean, M. Devlin, J. Dobaczewski, P.-H. Heenen, H.-Q. Jin, D. R. LaFosse *et al.*, Phys. Rev. Lett. **82**, 3763 (1999).

[3] T. Mizusaki, T. Otsuka, M. Honma, and B. A. Brown, Phys. Rev. C **63**, 044306 (2001).

[4] M. Horoi, B. A. Brown, T. Otsuka, M. Honma, and T. Mizusaki, Phys. Rev. C **73**, 061305(R) (2006).

[5] E. K. Johansson, D. Rudolph, L.-L. Andersson, D. A. Torres, I. Ragnarsson, C. Andreoiu, C. Baktash, M. P. Carpenter, R. J. Charity, C. J. Chiara *et al.*, Phys. Rev. C **77**, 064316 (2008).

[6] W. Satula, J. Dobaczewski, W. Nazarewicz, and M. Rafalski, Phys. Rev. C **81**, 054310 (2010).

[7] E. K. Johansson, D. Rudolph, I. Ragnarsson, L.-L. Andersson, D. A. Torres, C. Andreoiu, C. Baktash, M. P. Carpenter, R. J. Charity, C. J. Chiara, J. Ekman *et al.*, Phys. Rev. C **80**, 014321 (2009).

[8] C. Andreoiu, D. Rudolph, I. Ragnarsson, C. Fahlander, R. A. E. Austin, M. P. Carpenter, R. M. Clark, J. Ekman, R. V. F. Janssens, T. L. Khoo *et al.*, Eur. Phys. J. A **14**, 317 (2002).

[9] D. Rudolph, B. G. Carlsson, I. Ragnarsson, S. Åberg, C. Andreoiu, M. A. Bentley, M. P. Carpenter, R. J. Charity, R. M. Clark, M. Cromaz *et al.*, Phys. Rev. Lett. **96**, 092501 (2006).

[10] J. Gellanki, I. Ragnarsson, D. Rudolph, C. E. Svensson, L.-L. Andersson, C. Andreoiu, C. Baktash, M. P. Carpenter, R. J. Charity, C. J. Chiara *et al.*, Phys. Rev. C **80**, 051304(R) (2009).

[11] J. Gellanki, B. G. Carlsson, I. Ragnarsson, and D. Rudolph, Phys. Rev. C **89**, 024301 (2014).

[12] J. Ekman, D. Rudolph, C. Fahlander, I. Ragnarsson, C. Andreoiu, M. A. Bentley, M.P. Carpenter, R.J. Charity, R. M. Clark, M. Cromaz *et al.*, Phys. Rev. C **66**, 051301(R) (2002).

[13] D. Rudolph, C. Baktash, M. J. Brinkman, M. Devlin, H.-Q. Jin, D. R. LaFosse, L. L. Riedinger, D. G. Sarantites, and C. H. Yu, Eur. Phys. J. A **4**, 115 (1999).

[14] Y. Dong and H. Junde, Nucl. Data Sheets **121**, 1 (2014).

[15] C. J. Lister, J. W. Olness, and I. P. Johnstone, Phys. Rev. C **18**, 2169 (1978).

[16] H. Junde, Nucl. Data Sheets **110**, 2689 (2009).

[17] G. Guillaume, P. Fintz, A. Gallmann, F. Jundt, I. Riedinger-Ordoñez, and P. Sioshansi, Nucl. Phys. A **322**, 189 (1979).

[18] I.-Y. Lee, Nucl. Phys. A **520**, c641 (1990).

[19] M. Devlin, L. G. Sobotka, D. G. Sarantites, and D. R. LaFosse, Nucl. Instr. Meth. A **383**, 506 (1996).

[20] D. G. Sarantites, P.-F. Hua, M. Devlin, L. G. Sobotka, J. Elson, J. T. Hood, D. R. LaFosse, J. E. Sarantites, and M. R. Maier, Nucl. Instr. Meth. A **381**, 418 (1996).

[21] D. G. Sarantites, W. Reviol, C. J. Chiara, R. J. Charity, L. G. Sobotka, M. Devlin, M. Furlotti, O. L. Pechenaya, J. Elson, P. Hausladen *et al.*, Nucl. Instr. Meth. A **530**, 473 (2004).

[22] J. Ekman, D. Rudolph, C. Andreoiu, C. Fahlander, M. N. Mineva, M. A. Bentley, S. J. Williams, R. J. Charity, E. Ideguchi, W. Reviol *et al.*, Phys. Rev. C **70**, 014306 (2004).

[23] J. Ekman, Ph.D. thesis, Lund University, 2004, https://portal.research.lu.se/portal/en/publications/mirror-nuclei--isospin-symmetry-breaking-in-the-mass-a35-and-a51-mirror-nuclei(9d3df0c5-abb2-403b-af5d-ca0449065081).html.

[24] R. du Rietz, S. J. Williams, D. Rudolph, J. Ekman, C. Fahlander, C. Andreoiu, M. Axiotis, M. A. Bentley, M. P. Carpenter, C. Chandler *et al.*, Phys. Rev. C **72**, 014307 (2005).

[25] D. C. Radford, Nucl. Instr. Meth. A **361**, 297 (1995).

[26] J. Theuerkauf, S. Esser, S. Krink, M. Luig, N. Nicolay, O. Stuch, and H. Wolters, program TV, University of Cologne (unpublished).

[27] C. E. Svensson, J. A. Cameron, S. Flibotte, G. Gervais, D. S. Haslip, J. M. Nieminen, J. C. Waddington, J. N. Wilson, G.C. Ball, A. Galindo-Uribarri *et al.*, Nucl. Instr. Meth. A **396**, 228 (1997).

[28] E. Caurier, shell model code ANTOINE, IRES, Strasbourg, 1989–2002.

[29] E. Caurier and F. Nowacki, Acta Phys. Pol. B **30**, 705 (1999).

[30] A. Poves, J. Sánchez-Solano, E. Caurier, and F. Nowacki, Nucl. Phys. A **694**, 157 (2001).

[31] E. Caurier, G. Martinez-Pinedo, F. Nowack, A. Poves, and A. P. Zuker, Rev. Mod. Phys. **77**, 427 (2005).

[32] J. Ekman, C. Fahlander, and D. Rudolph, Mod. Phys. Lett. A **20**, 2977 (2005).

[33] M. A. Bentley and S. M. Lenzi, Prog. Part. Nucl. Phys. **59**, 497 (2007).

[34] M. Honma, T. Otsuka, B. A. Brown, and T. Mizusaki, Phys. Rev. C **65**, 061301(R) (2002).

[35] R. du Rietz, J. Ekman, D. Rudolph, C. Fahlander, A. Dewald, O. Möller, B. Saha, M. Axiotis, M. A. Bentley, C. Chandler *et al.*, Phys. Rev. Lett. **93**, 222501 (2004).

[36] D. Rudolph, K. P. Lieb, and H. Grawe, Nucl. Phys. A **597**, 298 (1996).

[37] D. Rudolph, R. Hoischen, M. Hellström, S. Pietri, Zs. Podolyák, P. H. Regan, A. B. Garnsworthy, S. J. Steer, F. Becker, P. Bednarczyk *et al.*, Phys. Rev. C **78**, 021301(R) (2008).

[38] P. Banerjee, B. Sethi, M. B. Chatterjee, and R. Goswami, Phys. Rev. C **44**, 1128 (1991).

[39] T. Bengtsson and I. Ragnarsson, Nucl. Phys. A **436**, 14 (1985).

[40] A. V. Afanasjev, D. B. Fossan, G. J. Lane, and I. Ragnarsson, Phys. Rep. **322**, 1 (1999).

[41] B. G. Carlsson and I. Ragnarsson, Phys. Rev. C **74**, 011302(R) (2006).